

POLITECNICO DI TORINO

Corso di Laurea Magistrale
in Ingegneria Energetica e Nucleare

Tesi di Laurea Magistrale
Reduction of the parasitic heat load to the Toroidal Field
magnets in the future European DEMO fusion machine



Relatore
Prof. Laura Savoldi
Dr. Roberto Bonifetto

Candidato
Sofia Viarengo

Anno accademico 2019/2020

Abstract

Nuclear fusion represents one of the main challenges in the energy field, and the DEMO machines under development in several countries worldwide will be the first fusion reactors able to produce electricity, although not at commercial level. In Europe, the EUROfusion Consortium is taking care of designing the EU-DEMO, strongly relying on the ITER experience.

The use of superconducting (SC) magnets is fundamental for the achievement of the huge electromagnetic fields necessary for the magnetic confinement of the plasma in DEMO. The use of superconductors at Low Critical Temperature (LCT) such as NbTi and/or Nb₃Sn is envisaged. The consequent requirement for the magnet system is to maintain the magnets at a temperature of ~ 4.5 K, to preserve the magnet SC state. The active cooling at 4.5 K by Supercritical Helium (SHe) is purposely used and systematic studies on the refrigeration of the SC winding packs in normal and off-normal operation are being carried out by several Institutions in Europe. Even though the SC magnet structure is contained in a cryostat and it is thermally shielded, parasitic thermal loads reach the SC magnets from the surrounding environment. The aim of this thesis work is the analysis and minimization of the parasitic thermal load reaching the Toroidal Field (TF) magnets of the EU-DEMO reactor through the two different channels of conduction, which are the gravity support (GS) and the Cryostat FeedThroughs (CFT) subject to parasitic heating of the coolant passing through them to reach the winding pack.

The GS is made to support vertically the total weight and resisting to out-of-plane electromagnetic loads. Unfortunately, it acts as a thermal bridge from the external environment to the magnet casing and SC winding pack. The challenge of the minimization of the heat load entering the TF coil casing by conduction from the GS is faced applying a Thermal Anchor (TA) with an active cooling of SHe at 4.5 K, re-routed from the coil casing cooling. A fully 3D model of the GS is developed using the commercial software STAR-CCM+ (Siemens PLM Software, Plano TX, U.S.A., [1]), which accounts for radiation to the surrounding structures, as well as for convective heat transfer to the coolant of the TA and conductive heat transfer to the coil casing. The model allows to optimize the vertical position of such a thermal anchor, and to return the minimum load to the casing of the TF coils. It is shown that the location of the TA closer to the casing globally reduces the thermal gradient across the GS, minimizing not only the load to the casing, but also the load globally entering the GS. A thermo-mechanical 2D analysis has been performed based on the computed temperature field, to check that the secondary stresses induced by the thermal gradient do not introduce mechanical issues in the GS. Different options, which consider a different amount of He flow re-routed from the TF casing, has been investigated, as well as the beneficial effect of introducing a second, standard TA at the thermal shield temperature (80 K).

The CFT are ~ 20 m long vacuum ducts, where a thermal shield embeds the containment duct for the He supply lines. They bring the SHe from a room temperature environment to the cold magnet environment. The He lines, in their actual design stage for DEMO, have been also studied with a simple 1D model along the pipe, complemented with dedicated 2D analyses where a conductive contribution comes from specific components such as the Vacuum Barrier at the beginning of the He line or the Cold Mass support, which bare the weight of containment duct every few meters of the lines. It has been shown that an active

cooling of the containment duct, as well as the introduction of a thermal intercept to thermally shield the Vacuum Barriers, are mandatory to reduce the temperature increase in the He lines below 10 mK.

Contents

List of Figures	iii
List of Tables	vi
Abbreviations	vii
1. Introduction	1
1.1. Nuclear Fusion reactors	1
1.2. Toroidal field coils and their auxiliary components	4
1.3. The issue of the parasitic heat load from the environment	6
1.4. Aim of the study	7
2. Gravity Support analysis	8
2.1. Design and geometry	8
2.2. Model setup	9
2.2.1. Thermal boundary conditions	10
2.2.2. Mechanical constraints	12
2.3. Results for the base case (no thermal anchors)	13
2.3.1. Thermal analysis results	13
2.3.2. Thermal-mechanical analysis results	15
2.4. First mitigation: Thermal Anchor application	16
2.4.1. Thermal analysis results	18
2.4.2. Thermal-mechanical analysis results	22
2.4.3. Parametric study: variable helium temperature	24
2.5. Second mitigation: Double Thermal Anchor application	26
2.5.1. Thermal analysis results	26
2.5.2. Thermal-mechanical analysis results	27
2.6. Preliminary conclusions	27
3. Magnet system feeders analysis	29
3.1. Design	29
3.2. Thermal model	32
3.2.1. Results	37
3.3. Preliminary conclusions	39
4. Conclusions	40
4.1. Future perspectives	41
Appendix 1: Physical properties of Stainless Steel and insulation material	42
Appendix 2: Modeling the heat transfer by radiation for the GS	44
Appendix 3: Construction of meshes	47
Appendix 4: Evaluation of the heat transfer coefficient to the TA pipes	50

Bibliography52

List of Figures

Figure 1.1 Cross section for fusion reactions from [6].....	2
Figure 1.2 Scheme of a Tokamak from [10].....	4
Figure 1.3 Sketch of a TF coil system [9].....	5
Figure 1.4 a) ENEA CICC for the innermost layer of the EU-DEMO TF WP and cross section highlighting the components reported in [12] and b) ENEA design of the innermost layer of EU-DEMO TF WP reported in [13].....	5
Figure 1.5 Simple sketch of the parasitic thermal load reaching the TF coil magnets. 1: conductive load through the gravity support (in orange), 2: radiative/conductive load in the CFT (blue pipe on the bottom of the sketch), both to the He line and to the Bus Bar; 3: conductive load to the Bus-Bar [15].....	6
Figure 2.1 Gravity support configuration under investigation in the present analysis a) in axonometry and b) from top and lateral views.....	8
Figure 2.2 a) Detailed view of the GS design and b) cut section of the GS considered in the present analysis.....	9
Figure 2.3 Flow-chart reporting the process for the thermal-mechanical analysis.....	10
Figure 2.4 Initial thermal boundary conditions for the 3D thermal analysis of the GS.....	10
Figure 2.5 Mechanical constrains.....	12
Figure 2.6 Temperature maps for $T_{TS}=80$ K without refrigeration a) in 3D and b) in 2D of a cut section on xy.....	13
Figure 2.7 Sankey diagram: representation of partitioning of power leaving the GS without refrigeration.....	14
Figure 2.8 Displacement map considering $T_{ts}=80$ K with no refrigeration of the GS. The deformed geometry is represented on a 40:1 scale.....	15
Figure 2.9 a) Details of ITER GS from [18] and b) sketch of DEMO GS from [18].....	16
Figure 2.10 a) Sketch of the GS profile highlighting the zones in which the location of the TA has been assumed for the current analysis; b) Sketch reporting how the refrigeration occurs.....	17
Figure 2.11 Boundary conditions for the 3D thermal analysis of the GS considering the application of one thermal anchor.....	17
Figure 2.12 Temperature distribution with the TA at z1 (a) and at z9 (b) and $T_{TS}=80$ K.....	18
Figure 2.13. Computed heat flux entering the GS from the bottom, as a function of the vertical position of the TA.....	19
Figure 2.14 Radiative heat flux computed on the a) right side, b) front side, c) left side and d) back side of the GS, as a function of the vertical position of the TA.....	19
Figure 2.15. Heat flux removed by the TA, as computed at different vertical position of the TA for each T_{TS} temperature.....	20
Figure 2.16. Summary of the comparison between the computed power entering the GS from the bottom, and the computed power to the TA, for three different location of the TA and different temperatures of the TS.....	20

Figure 2.17. Top heat flux reaching the TF coil casing computed at different vertical position of the TA for each T_{TS} temperature.....	21
Figure 2.18 Sankey chart a) for thermal anchor at z_1 and b) for thermal anchor at z_9	22
Figure 2.19 Temperature map computed with $T_{TS}= 80$ K and TA at z_9 on the GS cross section selected for the thermo-mechanical calculation.....	23
Figure 2.20 Vertical deformation map computed for the TA located in z_9 . The deformed geometry is represented on a 40:1 scale.....	23
Figure 2.21. Trend of maximum deformation depending on the vertical position of the thermal anchor for each TS temperature.....	24
Figure 2.22 a) 2D temperature map of the GS computed on a xy cross section and c) 2D temperature map of the GS computed on a yz cross section. They refer to $T_{TS}=80$ K and $m_{min} = 18$ g/s.....	25
Figure 2.23 Boundary conditions for double thermal anchor problem.....	26
Figure 2.24 Temperature distribution computed for the GS with a double TA for $T_{TS}= 80$ K.....	27
Figure 2.25 Displacement. The deformed geometry is represented on a 40:1 scale.....	27
Figure 3.1 Sketch of the Cryostat Feed-Through (CFT) penetration at B4 level and L2 level in DEMO (reproduced from [23]).....	29
Figure 3.2 Sketch of the feeder systems reported in [24].....	30
Figure 3.3 Detailed view of the ITER CFT cross-section (reproduced from [22]).....	30
Figure 3.4 Detailed sketch of the cross section of the Cold mass support (a) and vacuum barrier (b) within an ITER CFT (reproduced from [22]).....	31
Figure 3.5 Detailed view of the Bus-Bar support (a) and cryolines support (b) within and ITER CFT (reproduced from [22]).....	32
Figure 3.6 Sketch of the energy balance across an element of the He supply line, having infinitesimal length. m is the helium mass flow rate, c_p is the specific heat at constant pressure, q' is the heat load per unit length [W/m], T is the temperature, x is the coordinate along the He pipe.....	32
Figure 3.7 Sketch of the thermal model implemented.....	33
Figure 3.8 Sketch of the simple radiative model for the He supply line. The factor “7x” accounts for the number of cryogenic lines at the same temperature, namely 7.....	33
Figure 3.9 2D model of the Cold Mass support, highlighting the boundary conditions for the steady-state thermal conduction problem. The boundary condition on the top of the structure is constrained at the internal Containment duct temperature T_3 (see Figure 3.8); the thermal shield temperature T_{T5} is imposed where the support is in contact with the thermal shield, and the room temperature is imposed at the bottom of the structure.....	35
Figure 3.10 - 2D model of the Vacuum barrier, highlighting the boundary conditions for the steady-state thermal conduction problem. The room temperature is imposed on the outer circle, the Thermal Shield temperature T_{T5} is imposed on the cooling channels of the thermal shield, and convective heat transfer to Helium at 4.5 K is imposed on the outer surface of the cryogenic lines inside the thermal shield.....	36

Figure 3.11 Computed temperature profile for the He along the supply line, accounting (a) and neglecting (b) the contribution of the additional heat load from the Vacuum Barrier.....	37
Figure 3.12 Temperature map computed for the Vacuum Barrier, with a thermal shield temperature of 80 K. The color bar reports values in K.....	38
Figure 4.1 Schematic view of one TF coil [30].....	44
Figure 4.2. View factor chart, from [31].....	45
Figure 4.3 a) Mesh for the 3D thermal analysis and b) zoom of the 3D mesh.....	47
Figure 4.4 a) Mesh for the 2D thermo-mechanical analysis and b) zoom of the 2D mesh.....	48
Figure 4.5 2D mesh for the Cold Mass Support implemented in FreeFEM++-cs.....	49
Figure 4.6 2D mesh for the Vacuum Barrier.....	49

List of Tables

Table 2.1 Summary of the powers.....	14
Table 2.2 Displacements for each TS temperature.....	15
Table 2.3. Summary of the thermal load to the TF casing.....	25
Table 2.4 Comparison of the thermal load between the application of one TA and two TAs.....	26
Table 3.1 Geometrical dimensions of quantities of interest for the present analysis.....	36
Table 3.2 – Computed duct temperature and additional heat load from each of the Cold Mass support and from the Vacuum Barrier, as a function of different plausible nominal temperature of the Thermal shield.....	38
Table 3.3 Thermal load to the TF coils for each TS temperature accounting and neglecting the VB contribution.....	39

Abbreviations

Symbols	Description	Units
α	Thermal expansion coefficient	1/°C
A	Area	m ²
c_p	Heat capacity	J/kg/K
d_{pipe}	Pipe diameter	m
ε	Emissivity	-
E	Young modulus	GPa
$F_{x \rightarrow y}$	View factor from x object to y	-
F_p	Weight force	MN
h	Heat transfer coefficient	W/m ² /K
h_{eq}	Equivalent heat transfer coefficient	W/m ² /K
k	Thermal conductivity	W/m/K
μ_{he}	Helium dynamic viscosity	Pa*s
\dot{m}	Mass flow rate	g/s
ν	Poisson coefficient	-
Nu	Nusselt number	-
p	Inlet pressure	Pa
Pr	Prandtl number	-
\dot{Q}	Thermal power	W
\dot{q}	Heat flux	W/m ²
ρ	Density	kg/m ³
R	Thermal resistance	K/W
Re	Reynolds number	-
σ	Stefan-Boltzmann constant	W/m ² /K ⁴
T	Temperature	K
U	Transmissivity	W/m ² /K
v	Velocity	m/s
z	Vertical coordinate	-

Subscripts	Description
Bottom	Bottom zone
Cond	Conduction
Conv	Convection
Eq	Equivalent
Heline	Helium line
In	Inner
Inlet	Inlet
Ins	Insulant
Min	Minimum
Max	Maximum
Out	Outer
Outlet	Outlet
Rad	Radiation
Top	Upper zone

Acronyms	Description
BB	Bus-bar
CF	Cryostat Feedthrough
CD	Containment Duct
CL	Current Lead
CMS	Cold Mass Support
CTB	Coil-Terminal Box
DB	Dry box
HTC	Heat transfer Coefficient
ICF	In-Cryostat Feeders
GS	Gravity Support
LCT	Low Critical Temperature
SBB	S-Bend Box
SHe	Supercritical Helium
SS	Stainless Steel

TA	Thermal Anchor
TF	Toroidal Field
TS	Thermal Shield
VB	Vacuum Barrier

Chapter 1

1. Introduction

In perspective of a carbon-free economy and of limited amount of fossil fuel availability, the research is driven towards new technologies that can ensure the supply of energy in a continuous and eco-sustainable way [2]. Among the new research objectives in the energy field, the optimization of production processes, the increase in efficiency of energy systems and diversification of energy sources, for instance renewable technologies and nuclear machines, are of preminent importance.

The penetration in the energy market of renewable sources, such as solar and wind power, is mainly limited by their intrinsic intermittence and non-programmability, thus requiring the coexistence in the grid of generators or storages of a comparable power. That may compromise the sustainability also from investment-cost point of view [3].

In this context, the nuclear power is becoming increasingly relevant. The nuclear fission is an important no carbon emitting resource, although radioactive waste and the severity of damage in the event of an accident should not be underestimated. Therefore, the interest in nuclear fusion arises from the remarkable energy content of the reactions which would return the construction of a chain of huge fusion power plants, being able to produce large amount of energy against a very limited production of radioactive waste, with half-life times not problematic (up to 100 years), and without pollutant emissions. Nonetheless, the technological complexity for sustaining the extreme conditions needed by the reaction represents the main challenge for the complete exploitation of the nuclear fusion energy.

The research is developing *DEMO (DEMOstration Power Plant)* machines with the purpose of demonstrating the possibility to produce electricity and to guarantee the safety and the environmental sustainability of the fusion energy production. The Europe plays an important role, especially in the last decade: the EUROfusion Consortium [4] is working on the design of *EU-DEMO*, relying heavily on *ITER (International Thermonuclear Experimental Reactors)* experience [5], scheduled to be in operations in the 2050s.

1.1. Nuclear Fusion reactors

The nuclear fusion reactions consist in the interaction of light nuclear species, which have the peculiarity of releasing energy when two nuclei are joined to form a heavier nucleus. In order for a fusion to take place, the nuclei must be close enough so that the strong nuclear force prevails over the coulombian repulsion; since all nuclei are positively charged, the energy needed to overcome the repulsion is so high that can be provided only by heating (10^8 K) and/or compression to very high pressure. Then fusion is more easily achieved with lighter elements.

Therefore, the technology of controlled fusion aims at the isotopes of the hydrogen atom, which corresponds to the maximum energy released in the fusion with respect to the lower energy required to overcome the coulombian barrier. The reactions taken as references are:



where D is deuterium, T is Tritium and He^3 is helium-3. The Eqs. (1.2) and (1.3) are the most interesting thanks to ubiquity and abundance of materials.

As regarding the Eq. (1.4), it would be of interest for the high value of energy gain and also for the fact that it does not produce neutrons, but He^3 is not artificially producible and it has a small availability in nature.

Another fundamental parameter to be considered for the choice of the fusion reaction on the basis of which to direct research for the definition of fusion technology, is the value of the cross section as a function of the energy of the interacting nuclei, see Figure 1.1.

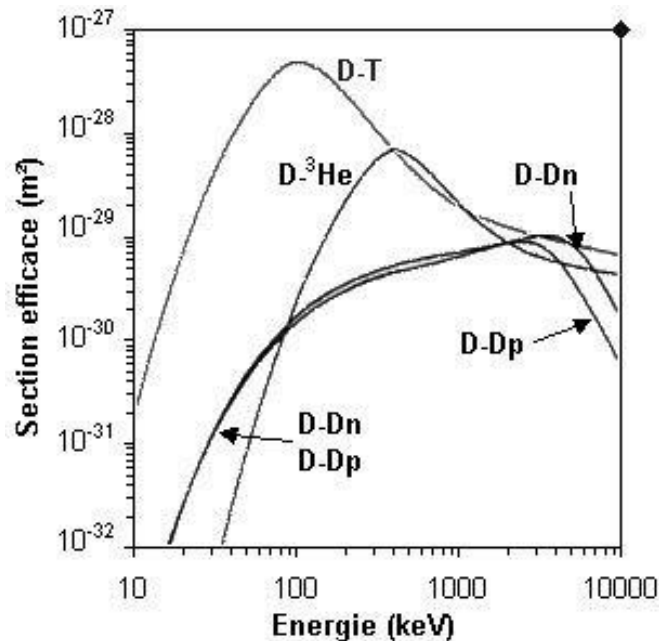


Figure 1.1 Cross section for fusion reactions from [6].

From Figure 1.1, it's possible to notice that D-T reaction, Eq. (1.1), is the characterized by the higher cross section and the lower energy threshold (~10 keV): therefore, both from the point of view of energy gain¹ (17.6 MeV) and

¹ Note that the 17.6 MeV value of the D-T reaction is theoretical, i.e. does not take into account the energy losses related to real processes, nor does it take into account the actual energy costs of tritium production.

the value of the section, it is the most interesting reaction. As a drawback, it requires to be produced starting from lithium isotopes (Li^6 and Li^7): therefore, energy is needed to sustain the extraction.

The technologies under development for the nuclear fusion reactors exploit D-T reaction: to reach the fusion, the mixture must be increased to 10^8 K, plasma state; a high plasma density (for increase the probability of collisions) must also be achieved, as well as a sufficiently long confinement time to trigger the fusion. According to the Lawson criterion, a fusion reaction is reached if:

$$n \cdot \tau_e \cdot T \geq 10^{21} \frac{\text{keV} \cdot \text{s}}{\text{m}^3} \quad (1.5)$$

where n is the plasma density, τ_e is the confinement time and T is the plasma temperature.

The use of conventional materials for the confinement is not conceivable, due to high temperatures achieved and intense radiative flux consequent. The main strategies are:

- *Inertial confinement*, based on the compression and consequent overheating of the fuel, by means of high power laser beams concentrated on a small and dense sphere with deuterium-tritium mixture, solid outside and gaseous inside.
- *Magnetic confinement*, a magnetic field is used to force the charged particles, particularly the deuterium and tritium ions, to follow trajectories on a plane perpendicular to the field itself; an appropriate series of induced magnetic fields keeps the plasma away from the walls of the fusion chamber.

Concerning the latter, different magnetic configurations has been studied, for instance:

- *Stellarator*, characterized by a triangular symmetry [7];
- *Tokamak*, characterized by a toroidal symmetry [8], see Figure 1.2.

A tokamak is a toroidal device characterized by a hollow envelope in which the plasma is confined by means of a magnetic field with spiral force lines. Its magnet system is constituted by: a central solenoid, acting as the primary of a transformer, driving the plasma current; vertical toroidal coils which generate a toroidal magnetic field for the plasma containment; horizontal poloidal coils which act as stabilizers, keeping the plasma in the center of the torus but they can also move it into the fusion chamber (vacuum vessel) in zones with different magnetic field values. Although intrinsically pulsed, tokamak devices should allow long plasma confinement times [9].

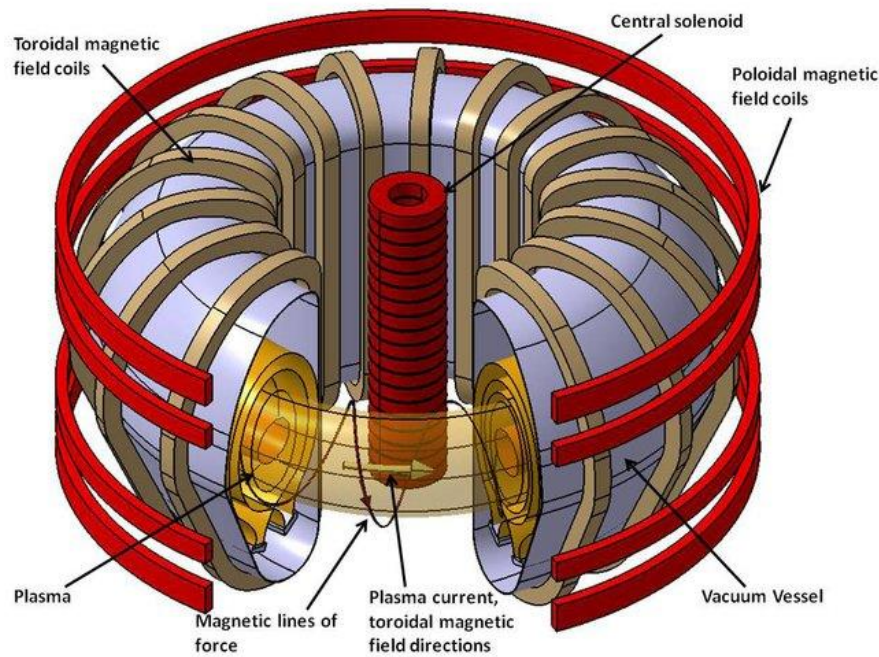


Figure 1.2 Scheme of a Tokamak from [10].

The magnetic system of the tokamak, encompassing the vacuum vessel where the plasma is contained, is entirely contained in the cryostat, a chamber at low temperature, to guarantee the superconductivity of the magnets.

The tokamak configuration characterized ITER, the biggest experimental reactor which aims at proving the feasibility of energy production from fusion [8]. Based on its design, DEMO reactor represents the next step in the path that will lead to commercial fusion power plant [5].

1.2. Toroidal field coils and their auxiliary components

The huge electromagnetic field necessary for magnetic confinement of plasma requires the application of superconducting (SC) magnets, for instance, at low critical temperature (LCT) such as NbTi and/or Nb₃Sn is envisaged. Due to the superconductivity, the Toroidal Field (TF) coils are one of the key points of the reactor performances: the low temperature of ~4.5 K must be preserved to maintain the magnet in SC state. Besides that, TF magnet system must be designed so that failures under off-normal operation cannot cause damage to the confinement barrier [11].

The DEMO TF magnets, Figure 1.3, according to the current design, are composed by a graded (Nb₃Sn) winding pack (WP) without radial plates, encapsulated in a steel casing [12]. The WP design proposed by ENEA in 2019 consists of double-layer wound rectangular cable-in conduit conductors (CICC), see Figure 1.4, to be cooled by Supercritical Helium (SHe) at 4.5 K and 0.6 MPa [12].

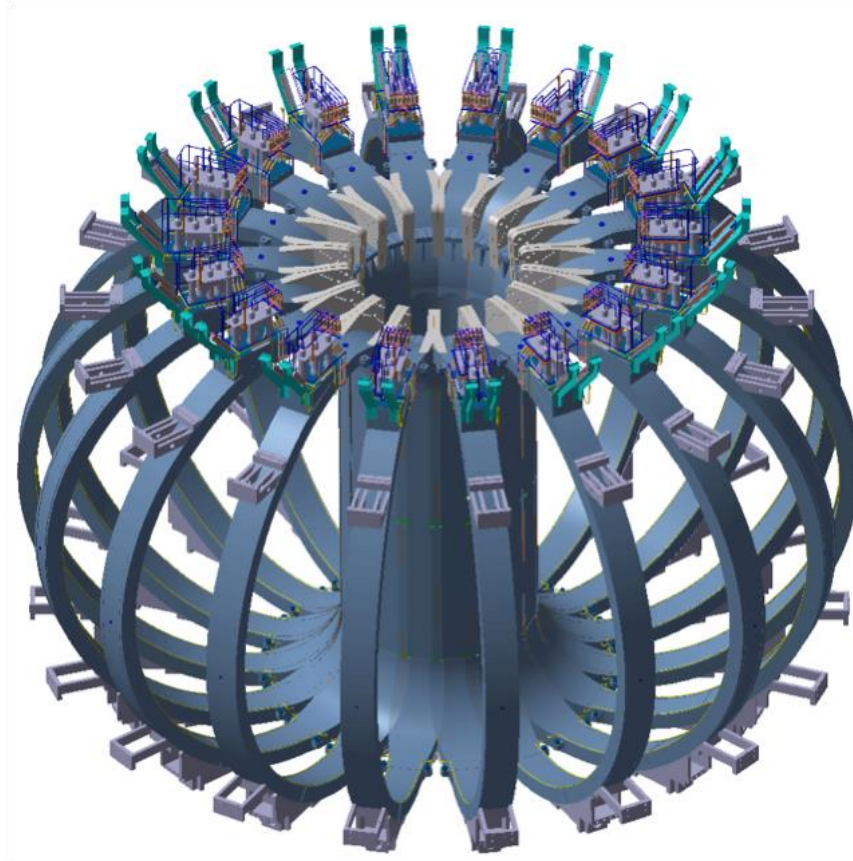


Figure 1.3 Sketch of a TF coil system [9].

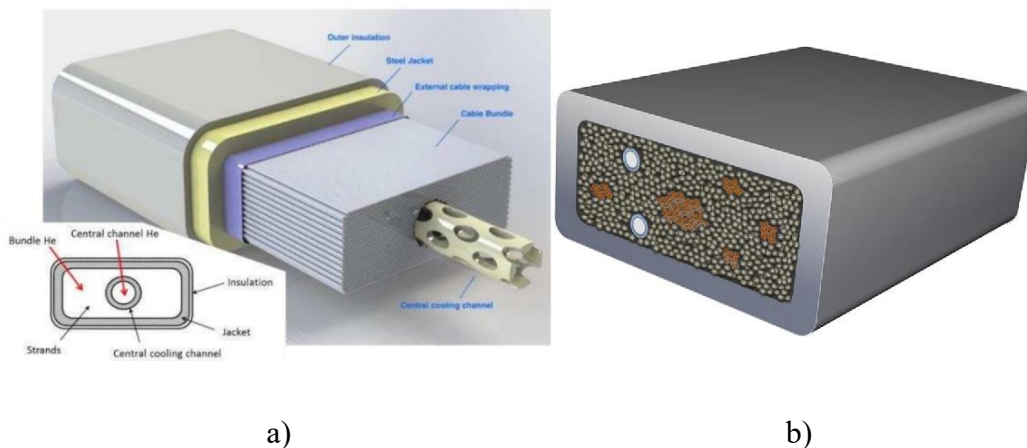


Figure 1.4 a) ENEA CICC for the innermost layer of the EU-DEMO TF WP and cross section highlighting the components reported in [12] and b) ENEA design of the innermost layer of EU-DEMO TF WP reported in [13].

The active cooling at 4.5 K by Supercritical Helium (SHe) is purposely used and systematic studies on the refrigeration of the SC winding packs in normal and off-normal operation are being carried out [14]. Even though the SC magnet structure is contained in a cryostat and it is thermally shielded, parasitic thermal loads reach the SC magnets from the auxiliary components with which it is in contact. The problem becomes more relevant considering that in the heat exchange at low temperature, the material properties are significantly influenced by every single watt exchanged, compromising their performances.

1.3. The issue of the parasitic heat load from the environment

The parasitic heat load reaches the TF magnets of the EU-DEMO reactor through the three different channels of conduction: the gravity support (GS), the Cryostat FeedThroughs (CFT) and the current leads (CL). The three act as thermal bridges from the external environment to the superconductor, see Figure 1.5.

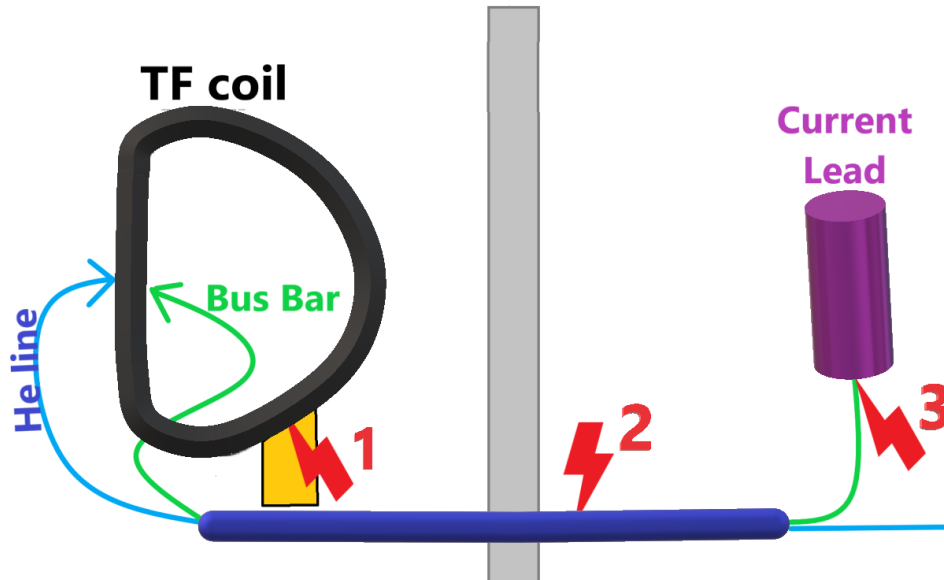


Figure 1.5 Simple sketch of the parasitic thermal load reaching the TF coil magnets. 1: conductive load through the gravity support (in orange), 2: radiative/conductive load in the CFT (blue pipe on the bottom of the sketch), both to the He line and to the Bus Bar; 3: conductive load to the Bus-Bar [15].

The GS is the structural element which sustains the TF magnets. It may be a channel for undesired heating of magnet casing and, from it, of the winding pack. It is subject to a huge temperature gradient from ambient temperature (300 K) to the SC one (4.5 K). Moreover, the gravity support holds the entire cold mass and the net downward force generated by the operation of the magnet.

The magnet system feeders, and in particular the long lines constituting the Cryostat FeedThrough (CFT), transport the cryogenic liquids to cool and control the temperature of the magnet system, and they connect the magnets to their power supply, housing the bus-bars (BBs). Furthermore, they allow the instrumentation channels, required for operation and monitoring the functioning of the coil system, to penetrate into the cryostat. Since they connect the SC with the external environment, they are subject to parasitic heating of the coolant passing through them from radiation and conductive thermal bridges; the heat load received from the helium is directly transported to the winding pack.

A third, minor, channel for the parasitic load income in the TF is through the current leads, which connect the BBs, penetrating inside the cryostat through the CFT, with the room-temperature power supply [16]. The income of heat occurs there by conduction at one end of the superconducting BB and by radiation along the BB, as for the He inlet lines, see above. The BBs are then connected to the magnet winding by (conductive) terminations, where the heat can be transferred to the winding pack.

1.4. Aim of the study

The purpose of this thesis work is to perform a first systematic analysis of the parasitic thermal load reaching the Toroidal Field (TF) magnets of the EU-DEMO reactor through two different channels of conduction, the gravity support (GS) and the Cryostat FeedThroughs (CFT).

Concerning the GS, after a first thermal analysis aimed at evaluating the heat load which could reach the TF coils without any dedicated refrigeration, two mitigation actions have been taken into account:

- the application of thermal anchor (TA) for refrigeration with helium at 4.5 K and the optimization of its position;
- the application of a second thermal anchor at a higher temperature (that of the thermal shield).

Moreover, a preliminary thermo-mechanical analysis has been implemented to evaluate the additional deformation that, on top of that caused by the cooldown of the machine, could be due to the thermal field originated by the TA.

As regarding the CFTs, the aim is to ensure that the helium that will cool the magnets does not undergo relevant temperature increases entering the WP. A 1D model has been developed for the advection of the He inside the longest cryo-line, which considers the effect of thermal radiation from the environment, together with the effect of the conductive contribution coming from localized thermal bridges located along the lines (Cold Mass support and Vacuum Barrier).

Chapter 2

2. Gravity Support analysis²

2.1. Design and geometry

The Gravity Support (GS) is made of an arrangement of parallel plates, see Figure 2.2, which allows the free radial displacement of the TF casing and simultaneously supports vertically the total weight and resists to out-of-plane electromagnetic loads.

The present analysis has been performed for the GS configuration of the EU-DEMO TF coil reported in [17] and for convenience in Figure 2.1.

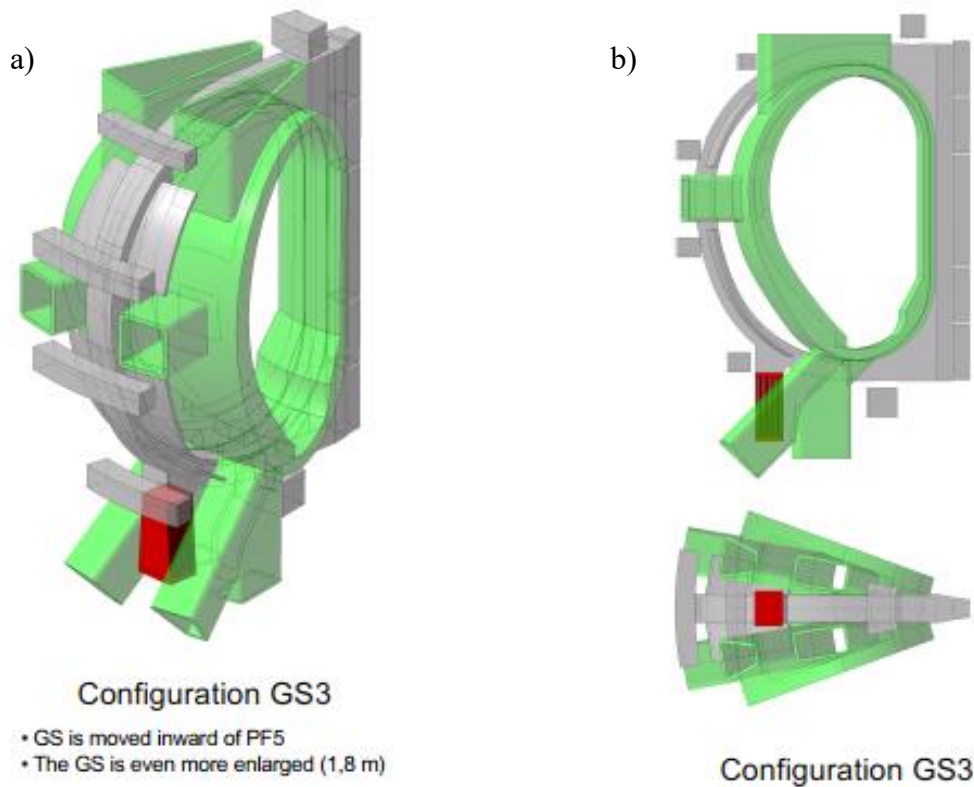


Figure 2.1 Gravity support configuration under investigation in the present analysis a) in axonometry and b) from top and lateral views.

The dimensioning of the GS for DEMO is based on ITER GS design: the differences consist in the size of the contact between the gravity support and the TF coil (consequently on the conductive path) and on the potential temperature of

² Mainly based on S. Viarengo, A. Allio and R. Bonifetto, "Support to the thermal-hydraulic design and analysis of the DEMO magnet system", EUROfusion report EFDA_D_2NZ98D, February 2020.

the TS, as stated in [18]. It is assumed it will be made of 304LN stainless steel, as in ITER.

The GS design is reported in Figure 2.2 a), specifying its dimensions, and in Figure 2.2 b) showing the cut section used for the mechanical analysis. It is characterized by 25 plates, each with a thickness of 36 mm and separated by gaps of 22.56 mm.

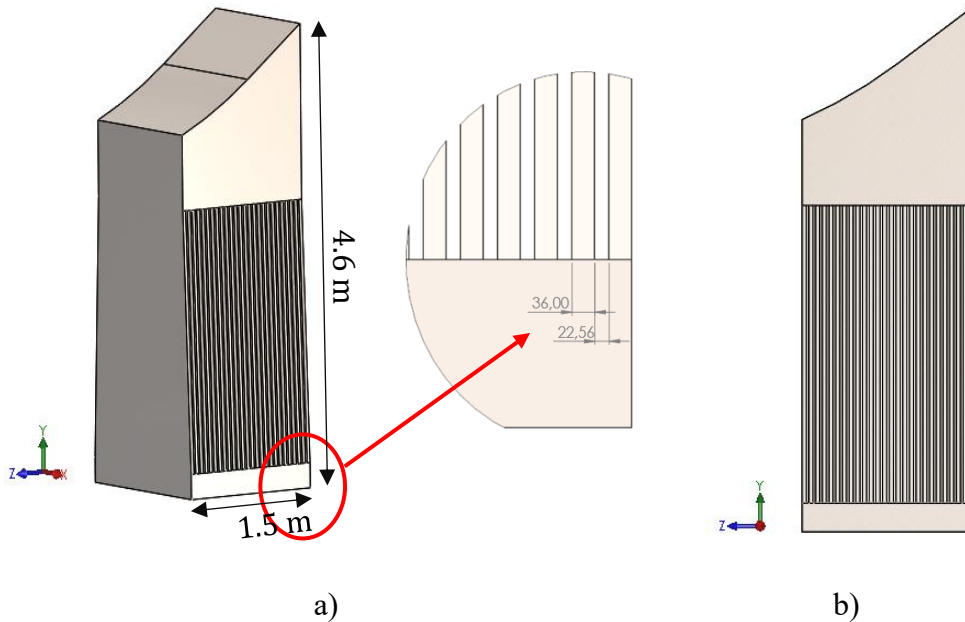


Figure 2.2 a) Detailed view of the GS design and b) cut section of the GS considered in the present analysis.

2.2. Model setup

In order to evaluate the amount of parasitic thermal load from GS to TF coils and to verify the mechanical deformation of the structure when a thermal anchor is applied, thermal analyses and thermal-mechanical analyses have been performed using the commercial software *STAR CCM+* (Siemens PLM Software, Plano TX, U.S.A., [1]).

A fully 3D finite volume thermal analysis has been implemented under steady-state conditions, varying parametrically the TS temperature from 80 K to 150 K, as stated in [18]; while the structural analysis has been performed with a 2D finite element study, on a vertical cut section, see Figure 2.2 b).

The thermal and the mechanical analyses have been performed separately and the thermal results are used to set-up the thermo-mechanical simulation, as reported in Figure 2.3.

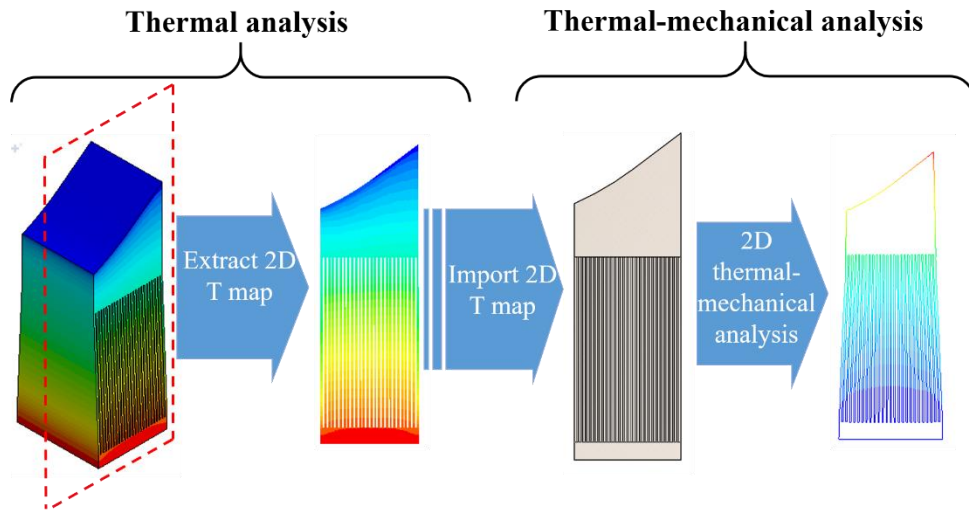


Figure 2.3 Flow-chart reporting the process for the thermal-mechanical analysis.

The SS properties are discussed in Appendix 1: Physical properties of Stainless Steel and insulation material, while the construction of meshes in Appendix 3: Construction of meshes.

2.2.1. Thermal boundary conditions

Regarding the thermal analysis, a steady state 3D simulation has been performed, first neglecting and then including the presence of one (or two) thermal anchors. The boundary conditions of the model are qualitatively sketched in Figure 2.4:

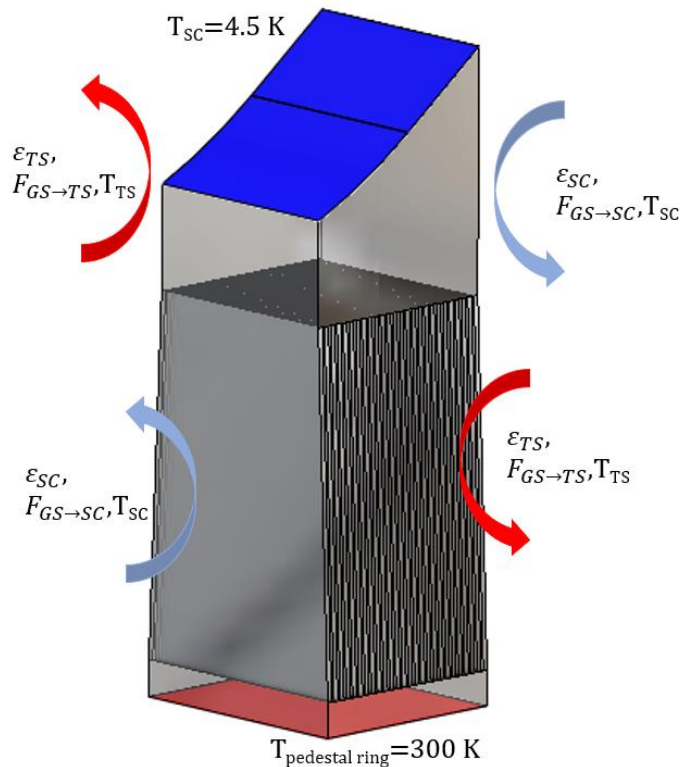


Figure 2.4 Initial thermal boundary conditions for the 3D thermal analysis of the GS.

As far as the boundary conditions are concerned:

- A *Dirichelet boundary condition* at a temperature of 4.5 K is imposed on the upper surface (most conservative hypothesis, considering the direct contact with the SC³);
- A *Dirichelet boundary condition* is imposed at the environmental temperature of 300 K on the pedestal ring;
- *Radiation boundary conditions* are imposed on any exposed surface (see Figure 2.1); therefore:
 - The external plate surfaces surrounded by the TS. The TS temperature is varied parametrically from 80 K to 150 K, considering the radiation between grey opaque diffusing surfaces as reported in Eq. (2.1)

$$\dot{Q} = \sigma \frac{1}{\frac{1 - \varepsilon_{TS}}{\varepsilon_{TS} \cdot A_{TS}} + \frac{1 - \varepsilon_{GS}}{\varepsilon_{GS} \cdot A_{GS}} + \frac{1}{A_{GS} \cdot F_{GS \rightarrow TS}}} (T_{GS}^4 - T_{TS}^4) [W] \quad (2.1)$$

In Eq. (2.1), $\sigma = 5.67 \cdot 10^{-8} \frac{W}{m^2 K^4}$ is the Stefan-Boltzmann constant, $\varepsilon_{GS} = 1$ is the GS emissivity (considering the gravity support as a black body), $\varepsilon_{TS} = 0.05$ is the emissivity of the silvered surface as reported in [18], $F_{GS \rightarrow TS} = 0.5$ is the view factor⁴ between the surfaces, A_{GS} is the area of the lateral surfaces of the object, A_{TS} is the area of the thermal shield which faces the GS, T_{GS} is the temperature of the external surfaces of the GS, $T_{TS} = 80 K$ is the TS temperature.

Due to the lack of information about the vacuum vessel dimension, the surface in Eq. (2.1) has been assumed around three times greater than the GS one. Managing the Eq. (2.1), it can be rewritten as Eq. (2.2), and the radiative heat flux as in Eq. (2.3):

$$\dot{Q} = \sigma \cdot \frac{3 \cdot \varepsilon_{TS} \cdot A_{GS} \cdot F_{GS \rightarrow TS}}{F_{GS \rightarrow TS} - \varepsilon_{TS} \cdot F_{GS \rightarrow TS} + 3 \cdot \varepsilon_{TS}} \cdot (T_{GS}^4 - T_{TS}^4) [W] \rightarrow \quad (2.2)$$

$$\dot{q} = \sigma \cdot \frac{3 \cdot \varepsilon_{TS} \cdot F_{GS \rightarrow TS}}{F_{GS \rightarrow TS} - \varepsilon_{TS} \cdot F_{GS \rightarrow TS} + 3 \cdot \varepsilon_{TS}} \cdot (T_{GS}^4 - T_{TS}^4) \left[\frac{W}{m^2} \right] \quad (2.3)$$

- The back and the front surfaces are facing the magnet (see Figure 2.1), approximated as a black body ($\varepsilon_{magnet} = 1$) at a temperature of 4.5 K, with a view factor⁵ assumed equal to

³ Actually, the GS is in direct contact with the TF coil casing which will have a temperature different from (larger than) 4.5 K.

⁴ The evaluations of the view factor are explained in Appendix 2: Modeling the heat transfer by radiation for the GS.

⁵ The back and the front surfaces view factors have been calculated separately due to different dimensions of the exposed face and the different mutual position.

0.4 (see Appendix 2: Modeling the heat transfer by radiation for the GS) for both parts.

Considering the radiation between two black surfaces in Eq. (2.4) and the radiative heat flux in Eq. (2.5):

$$\dot{Q} = \sigma \cdot F_{GS \rightarrow SC} \cdot A_{GS} \cdot (T_{GS}^4 - T_{SC}^4) [W] \rightarrow \quad (2.4)$$

$$\dot{q} = \sigma \cdot F_{GS \rightarrow SC} \cdot (T_{GS}^4 - T_{SC}^4) \left[\frac{W}{m^2} \right] \quad (2.5)$$

where $F_{GS \rightarrow SC}$ is the view factor between the surfaces (assumed here to be 0.4), A_{GS} is the area of the front and back surfaces of the object, T_{GS} is the temperature of the external surfaces of the GS, $T_{SC} = 4.5 K$ is the temperature of the magnet.

Note that the effect of the assumptions of view factors is very small due to limited role of radiative losses, see the results in 2.4.1.

The other surfaces are considered adiabatic.

2.2.2. Mechanical constraints

The GS is intended to sustain the weight of the TF coils and all the structures that will be hung to them, so that it will be affected by a huge vertical force: a linear elastic model has been considered with the purpose of computing the state of deformation to which it is subjected.

The applied forces are shown in Figure 2.5.

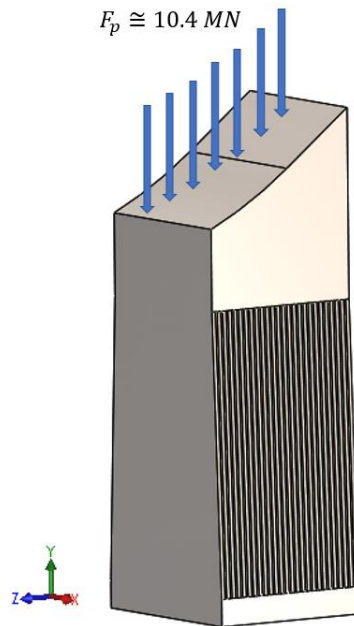


Figure 2.5 Mechanical constraints.

Note that all base points *are fixed*, and no mechanical constraints are applied on the other surfaces.

A *vertical distributed force* around 10.4 MN is applied on the top face corresponding to the weight of the structures that are on the GS [19].

The analysis has been performed applying the temperature map evaluated thanks to the thermal study, to the GS considered undeformed (i.e. the effect of the cooldown has not been taken into account, neither in terms of additional deformations, nor in terms of induced stresses).

2.3. Results for the base case (no thermal anchors)

In this section a thermal and a thermal-mechanical analysis is reported considering the GS without any thermal anchor. The purpose of this first analysis is the evaluation of the parasitic thermal load that may reach the TF coils and the deformation induced by the thermal field in the gravity support.

2.3.1. Thermal analysis results

The boundary conditions are represented in Figure 2.4 and the 3D simulation in steady state has been carried out for each of the different values of TS temperature investigated here.

In Figure 2.6 a) and b) the 3D temperature map for TS equal to 80 K and its cut section are reported respectively.

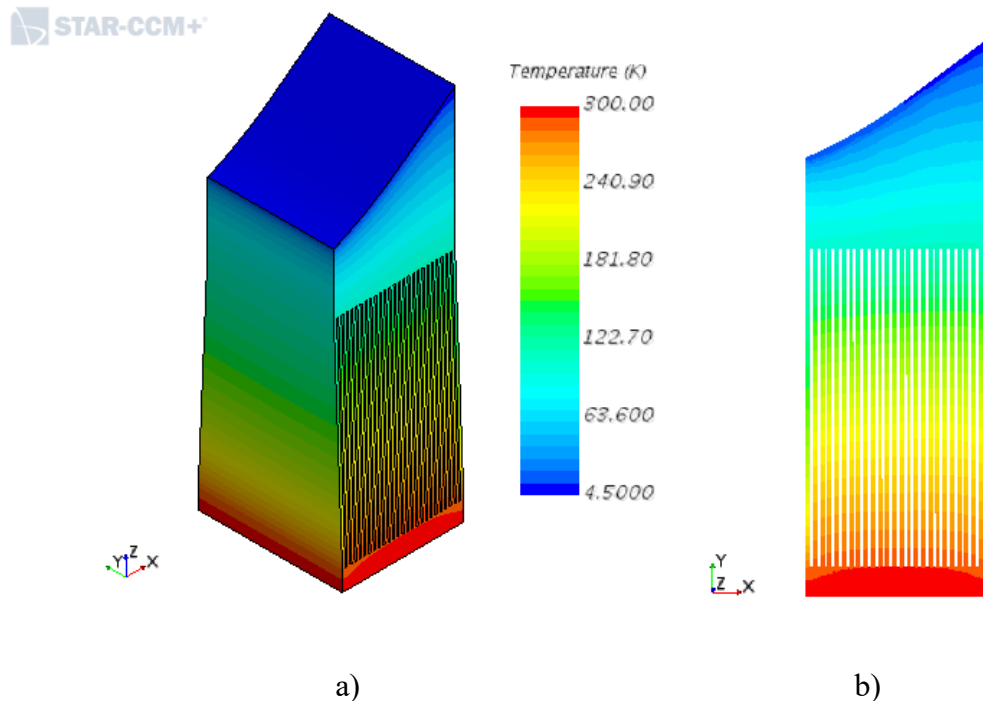


Figure 2.6 Temperature maps for $T_{TS}=80$ K without refrigeration a) in 3D and b) in 2D of a cut section on xy .

The GS is subject to a temperature gradient between 300 K and 4.5 K, influenced only by heat dissipation due to the radiation towards the surrounding environment, which removes around 28% of the entering power (see Figure 2.7).

From Figure 2.6 b), it's possible to notice the radiation effects: they will be greater on the lower zone of the GS, characterized by a higher temperature, in fact the temperature isolines are inclined at the edges; on the upper zone, instead, the radiation effects are weaker, thus the isolines are more "horizontal" (the temperature gradient along x-axis is lower). Moreover, since the external environment is at lower temperature with respect to the high temperature zone, the heat will be transferred *from* the GS.

The results obtained from the simulation show that the radiation has an impact approximately equal for each TS temperature, therefore the temperature maps are quite similar. The *Sankey diagram* in Figure 2.7 shows the power partitioning.

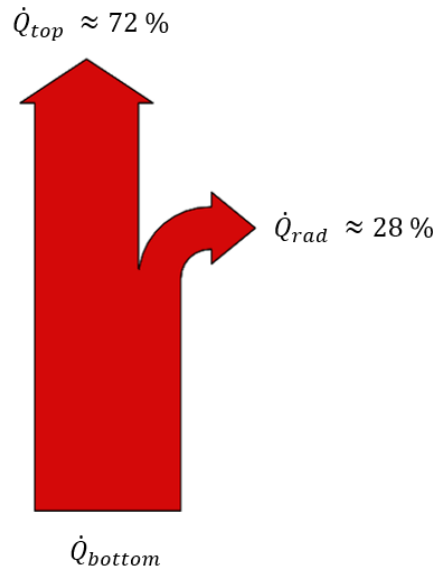


Figure 2.7 Sankey diagram: representation of partitioning of power leaving the GS without refrigeration.

where:

- \dot{Q}_{top} represents the portion reaching the casing;
- $\dot{Q}_{radiation}$ represents the portion dissipated by radiation to the other components a lower temperature;
- \dot{Q}_{bottom} represents the heat entering the domain.

Table 2.1 summarizes the entering power, the dissipated power by radiations and the heat load reaching the TF coil casing:

Table 2.1 Summary of the powers

T_{TS} [K]	\dot{Q}_{bottom} [W]	\dot{Q}_{rad} [W]	\dot{Q}_{top} [W]
80	1822.7	524.3	1296.1
120	1820.0	514.2	1300.7
150	1810.4	496.7	1312.9

The power reaching the TF coils without refrigeration is around 1.3 kW (~ 70% of the entering power): that amount could have a large impact on the SC

performances. Therefore, an active cooling of the structure aiming at the reduction of that significant load could help in reducing the burden on the cooling loop of the winding pack or casing.

2.3.2. Thermal-mechanical analysis results

Referring to the mechanical constraints reported in Figure 2.5, a 2D mechanical analysis has been carried out starting from the 2D temperature map computed in the thermal simulation, see Figure 2.6 b). Due to the symmetry of the problem and the onerous computational cost of a 3D mechanical simulation, a 2D study was judged sufficient for the intended purpose. The objective of the thermal-mechanical analysis is to verify the structural stability of the GS subject to a huge vertical force: namely, if it can resist to the buckling.

The displacement map is reported in Figure 2.8:

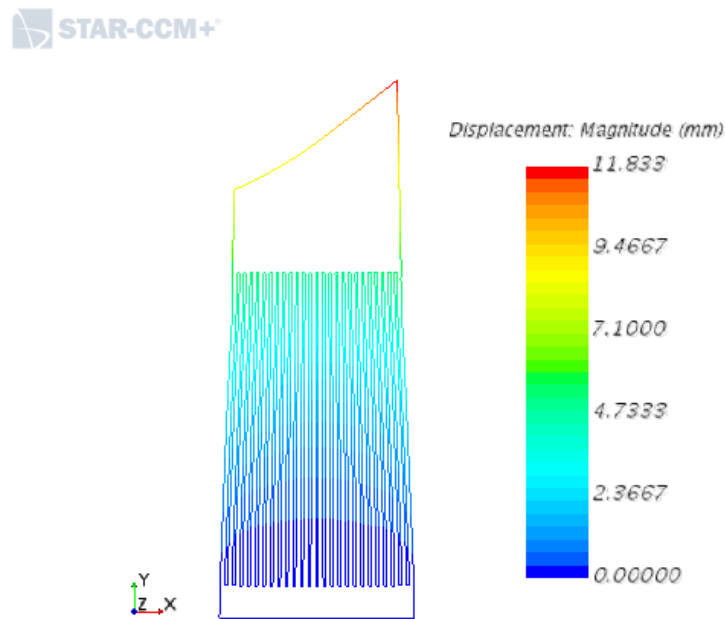


Figure 2.8 Displacement map considering $T_{ts}=80$ K with no refrigeration of the GS. The deformed geometry is represented on a 40:1 scale.

The maximum displacement is independent on the TS temperature as reported in Table 2.2.

Table 2.2 Displacements for each TS temperature

T_{TS} [K]	Maximum displacement (mm)
80	11.83
120	11.82
150	11.80

It is possible to see in Figure 2.8 that the GS is subjected to a contraction, due to the mechanical load, and a restriction in the upper zone, due to the low temperature. Furthermore, no horizontal displacement takes place, in view of the assumption on the perfect vertical direction of the load on the GS.

2.4. First mitigation: Thermal Anchor application

In this section, a thermal analysis and a thermal-mechanical analysis of a first mitigation, constituted by the application of a thermal anchor (TA) surrounding the GS (starting from ITER design [20]), is presented (see Figure 2.9).

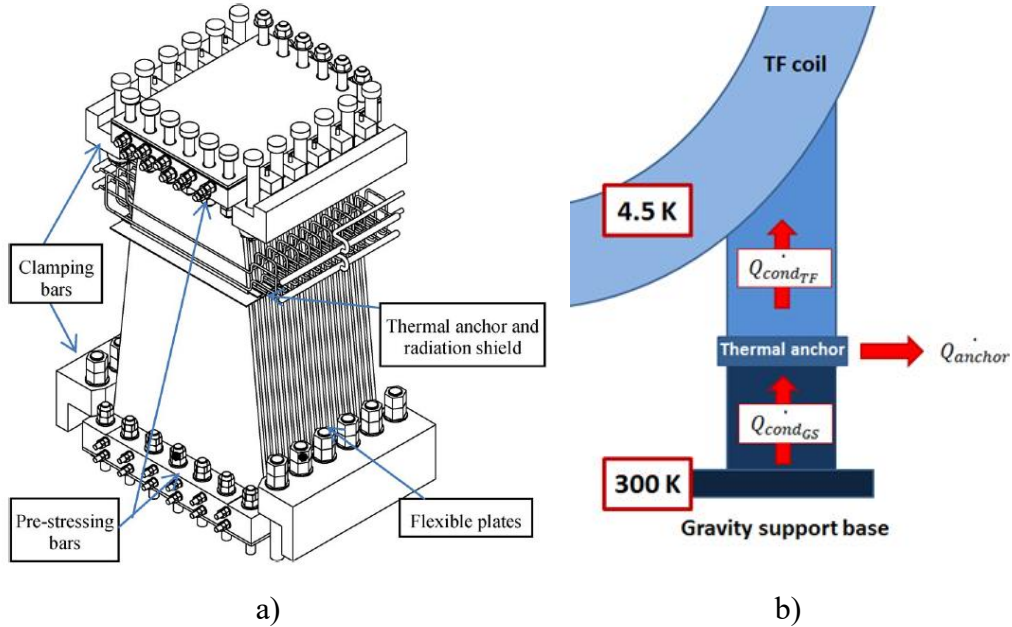


Figure 2.9 a) Details of ITER GS from [18] and b) sketch of DEMO GS from [18].

The GS should be cooled down in order to minimize the heat which inevitably could be transferred from the base to the TF coils: the purpose of the analysis is to determine the optimal position, along the GS height, of the refrigeration pipes. The cooling fluid is helium at 4.5 K, which is assumed to be diverted from the TF case cooling loop. This study is carried out for the three temperatures of the TS.

The refrigeration is assumed occurring through 20 mm outer diameter pipes interposed between the plates, see Figure 2.10 b). Nine different positions for the TA along the vertical coordinate z have been considered, each characterized by a height of 20 mm, see Figure 2.10 a):

- 1) $z_1 = 0.42 - 0.44 \text{ m}$
- 2) $z_2 = 0.70 - 0.72 \text{ m}$
- 3) $z_3 = 0.98 - 1.00 \text{ m}$
- 4) $z_4 = 1.26 - 1.28 \text{ m}$
- 5) $z_5 = 1.54 - 1.56 \text{ m}$
- 6) $z_6 = 1.82 - 1.84 \text{ m}$
- 7) $z_7 = 2.10 - 2.12 \text{ m}$
- 8) $z_8 = 2.38 - 2.40 \text{ m}$
- 9) $z_9 = 2.66 - 2.68 \text{ m}$

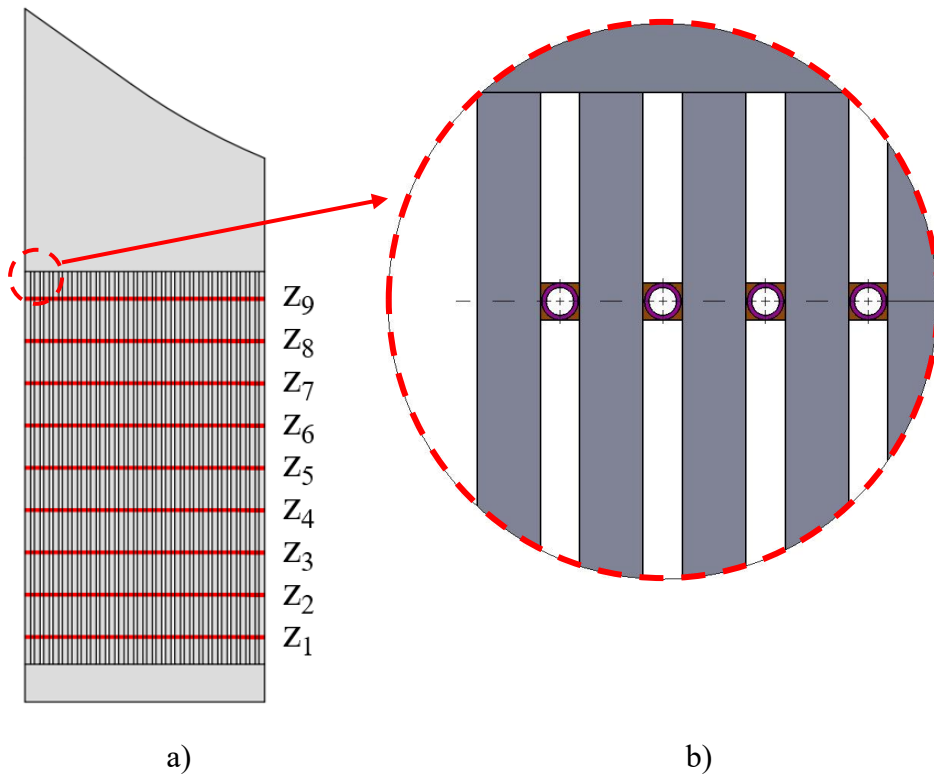


Figure 2.10 a) Sketch of the GS profile highlighting the zones in which the location of the TA has been assumed for the current analysis; b) Sketch reporting how the refrigeration occurs.

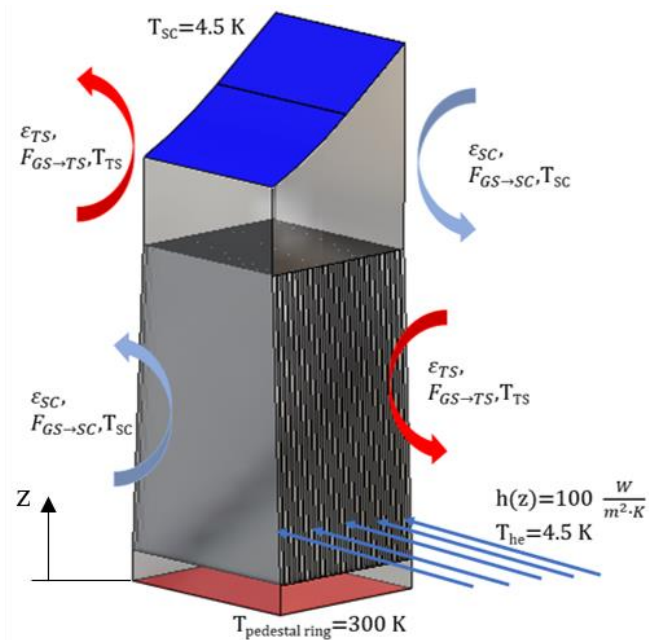


Figure 2.11 Boundary conditions for the 3D thermal analysis of the GS considering the application of one thermal anchor.

A Robin boundary condition has been added to simulate the TA: it is imposed only in one of the restricted areas considered along the z-axis through the plates with a temperature of 4.5 K, see Figure 2.11. The estimation of the equivalent heat transfer coefficient has been qualitatively implemented starting from the thermophysical properties of the helium evaluated at the inlet condition ($T = 4.5\text{ K}$ and $p = 600\text{ kPa}$) and the conductive resistance of the pipe in which it

flows through, both for the minimum and the maximum mass flow rate. Those two flow rates are respectively $\dot{m}_{min} = 18 \text{ g/s}$ (if only the SHe mass flow rate of the 12 CCCs cooling the back side of the casing outboard leg is rerouted to the GS cooling) and $\dot{m}_{max} = 145 \text{ g/s}$ (if the SHe mass flow rate of all the 96 CCCs cooling the casing is rerouted to the GS cooling) [21]. The details about the procedure for the estimation of the equivalent heat transfer coefficient are reported in Appendix 4: Evaluation of the heat transfer coefficient to the TA pipes, resulting in a tentative value of $100 \frac{\text{W}}{\text{m}^2 \cdot \text{K}}$.

2.4.1. Thermal analysis results

Temperature distributions regarding the two extreme positions of the TA ($z = z_1$ ad $z = z_9$, respectively) at TS temperature equal to 80 K are represented in Figure 2.12 a) and b).

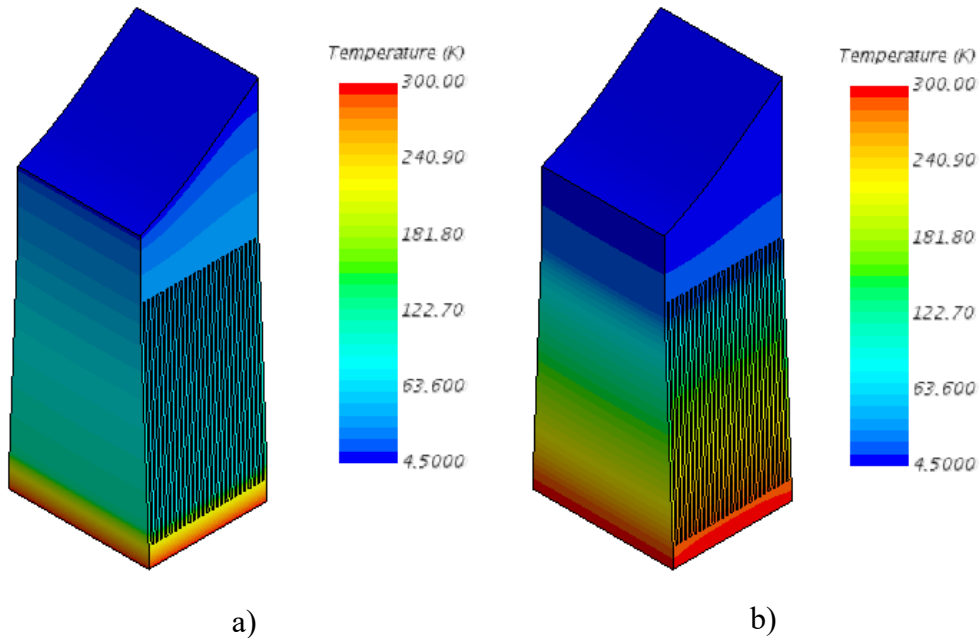


Figure 2.12 Temperature distribution with the TA at z_1 (a) and at z_9 (b) and $T_{TS}=80 \text{ K}$.

The higher the position of the thermal anchor, the greater is the zone at relatively high temperature: consequently, the contribution of the heat losses will be different.

Bottom heat flux (entering the domain)

In Figure 2.13, it is shown how the thermal power entering for the bottom of the GS is affected by the location of the thermal anchor, but not by the TS temperature. The reason is that the lower the refrigeration zone, the higher will be the thermal gradient because the shorter the length over which it is calculated; this is confirmed by the fact that the curves overlap assuming the same values regardless of the TS temperature, because principally it affects the radiation on the GS lateral sides, but it is negligible with respect to the other heat dissipation contributions.

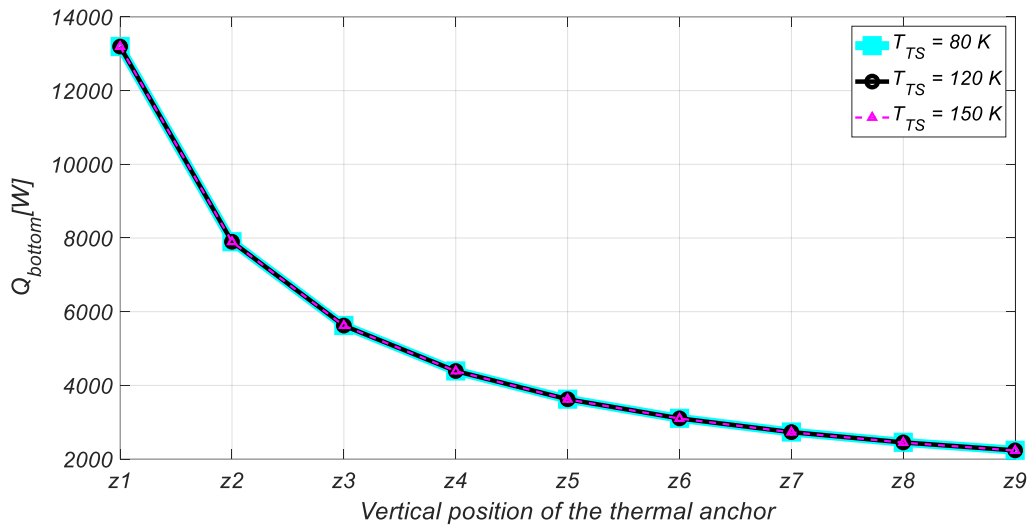


Figure 2.13. Computed heat flux entering the GS from the bottom, as a function of the vertical position of the TA.

Radiative heat flux (lateral sides)

In Figure 2.14, for each side of the gravity support the trend of the radiation, for three possible values of temperature of the cryostat, as a function of the refrigeration position is shown. The load removed by the coolant decreases as the location of the thermal anchor is moved upward. As expected, the radiative heat flux exchange on the front and the back sides are identical, because the coil is at unvaried temperature of 4.5 K, see Figure 2.14 b) and c). Instead, the other sides are influenced by the TS temperature. Note that in Figure 2.14 a) and d) where $T_{TS} = 150 K$, considering the configuration in which the cooling pipes are situated at z_1 the heat has negative sign: this is due to the fact that the GS temperature will be lower than the TS temperature, so the surrounding will heat up the GS.

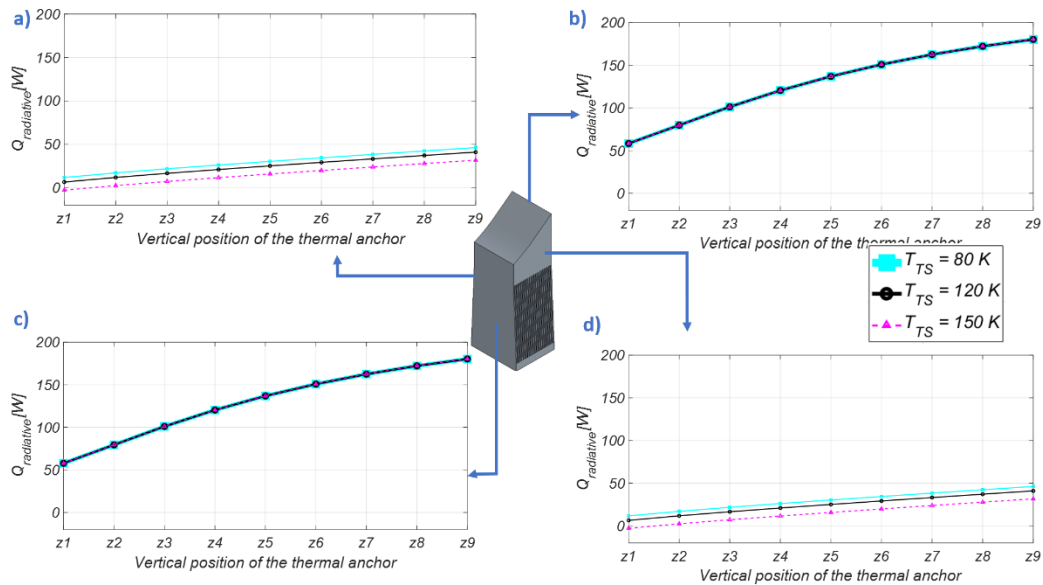


Figure 2.14 Radiative heat flux computed on the a) right side, b) front side, c) left side and d) back side of the GS, as a function of the vertical position of the TA.

Convective heat flux (removed by helium)

The trends of the heat removed by the helium is reported in Figure 2.15 and it has again a decreasing monotonic behavior. The heat transferred to the coolant from the GS removes most of the heat and, from simulations, it is completely independent on TS temperature, because the contributions related to the radiation are much smaller than the convective one.

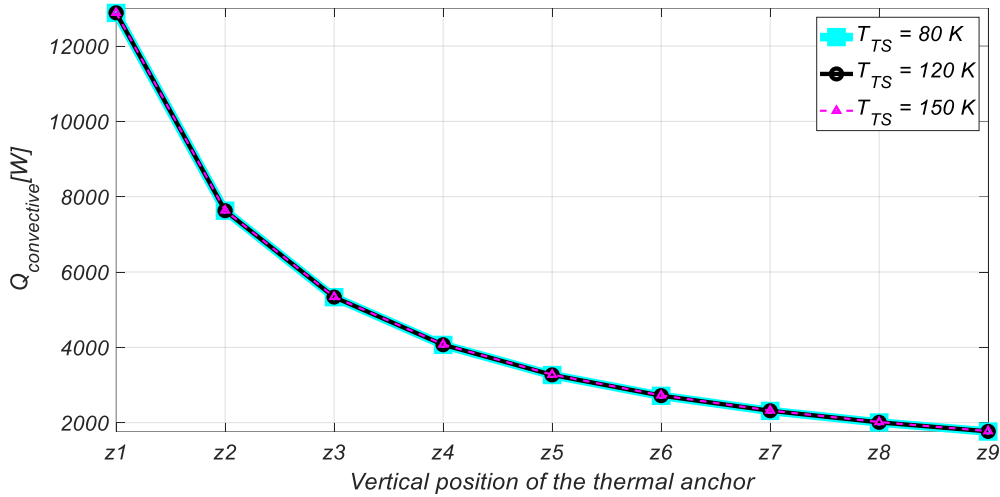


Figure 2.15. Heat flux removed by the TA, as computed at different vertical position of the TA for each T_{TS} temperature.

The power entering the domain and the corresponding convective heat flux to the TA are shown in Figure 2.16 confirming that, independently from the location of the TA, it takes care of the largest fraction of the heat entering the GS.

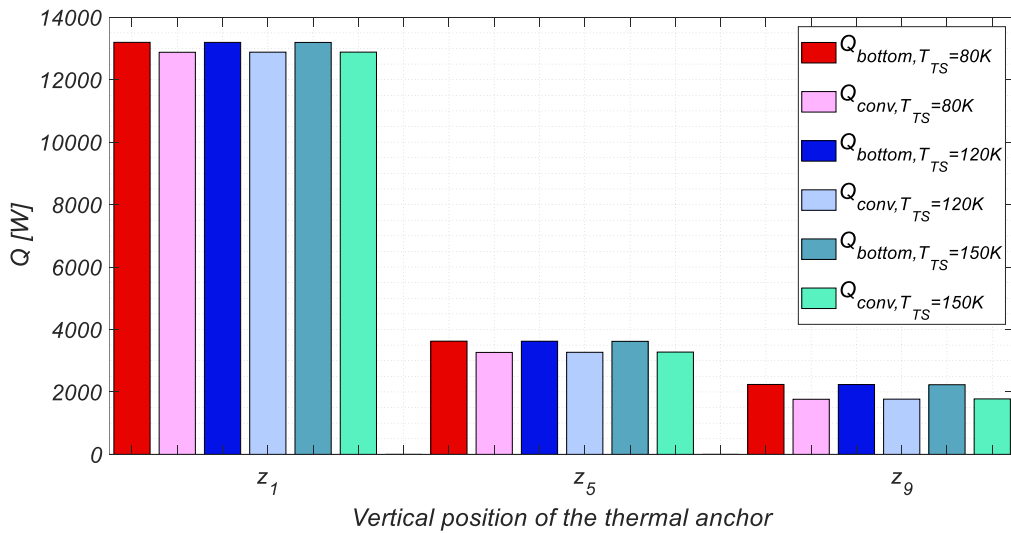


Figure 2.16. Summary of the comparison between the computed power entering the GS from the bottom, and the computed power to the TA, for three different location of the TA and different temperatures of the TS.

Top heat flux (reaching the casing)

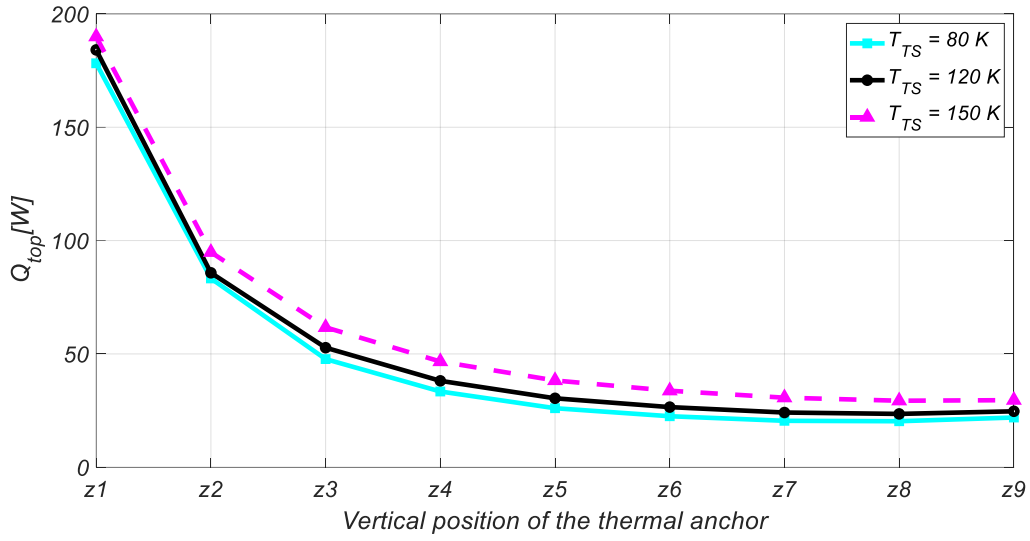


Figure 2.17. Top heat flux reaching the TF coil casing computed at different vertical position of the TA for each T_{TS} temperature.

The main parameter of interest of the study is the amount of heat that reaches the TF casing \dot{Q}_{top} that is shown in Figure 2.17. As the TA is moved upward, the heat flux transferred to the coil casing reduces, at least up to z_8 (note that at z_9 the thermal field is distorted due to the end of the parallel plates). Moreover, the lower the TS temperature, the higher is the amount of energy leaving the GS by radiation. Therefore, the minimum heat flux to the casing is given for pipes of the TA located at $z_8 = 2.38 - 2.40\text{ m}$ for all the possible different T_{TS} , among which the case corresponding to a TS temperature of 80 K shows the smallest load to the TF casing ($\sim 20\text{ W}$). That quantity has been significantly reduced with respect to the base case, two orders of magnitude lower.

However, it is necessary to note that the \dot{Q}_{top} difference between three cases for the TS temperature is inappreciable (around the 30%) compared to the strong variation that the thermal load has depending on the location of the TA (up to 600% in the worst cases). Concerning the choice of the optimal TA position, the z_9 becomes the most suited location since \dot{Q}_{top} at minimum TS temperature is $\sim 22\text{ W}$, almost the same load to TF casing for TA at z_8 , and furthermore it could ensure mechanical support to the piping.

The partition of the heat entering the domain has similar trend in each simulation, which independent on the TS temperature; it is qualitatively sketched in the *Sankey diagrams* in Figure 2.18, where:

- \dot{Q}_{top} is the portion reaching the casing;
- $\dot{Q}_{convection}$ is the heat removed by the helium at 4.5 K;
- $\dot{Q}_{radiation}$ is the portion dissipated by radiation to the other components a lower temperature;
- \dot{Q}_{bottom} is the heat entering the domain.

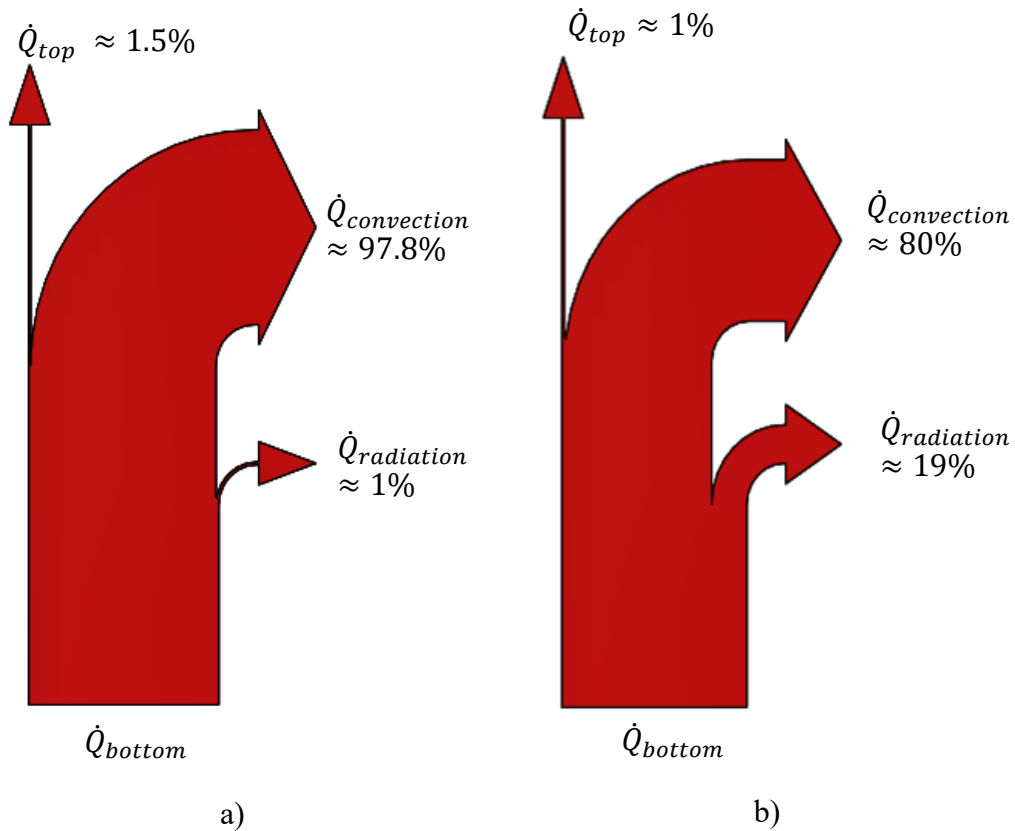


Figure 2.18 Sankey chart a) for thermal anchor at z_1 and b) for thermal anchor at z_0 .

The figures are related to the lowest Figure 2.18 a) and the highest zone Figure 2.18 b) in which the refrigeration may take place. The position of the TA influences the fraction of heat dissipated by convection and by radiation.

Thus, according to that thermal study, the minimum acceptable thermal load to the casing of $\sim 22 W$ is obtained for the TS at 80 K and the thermal anchor at z_0 . The load increases to $\sim 30 W$ when $T_{TS}=150 K$. The amount of the parasitic load is significantly reduced with respect to the base case without refrigeration, $\sim 1300 W$.

2.4.2. Thermal-mechanical analysis results

The 2D structural analysis has been implemented starting from the temperature map, see Figure 2.19, of a cut section in the middle of the geometry. The obtained deformation state could be added to those that will be due to cooldown, of which no information are available so far.

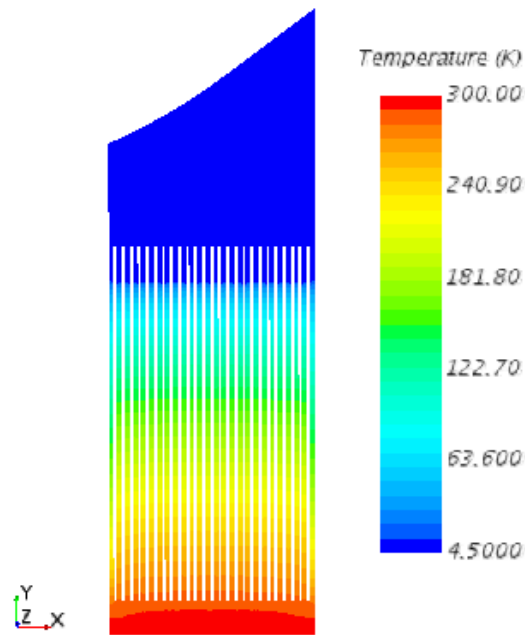


Figure 2.19 Temperature map computed with $T_{TS} = 80$ K and TA at z_9 on the GS cross section selected for the thermo-mechanical calculation.

The study has been carried out for each TS temperature and for each TA location. For the TA at the location z_9 and $T_{TS} = 80$ K, the temperature map used to enter the thermo-mechanical simulation is reported in Figure 2.19. The corresponding vertical deformation is reported in Figure 2.20.

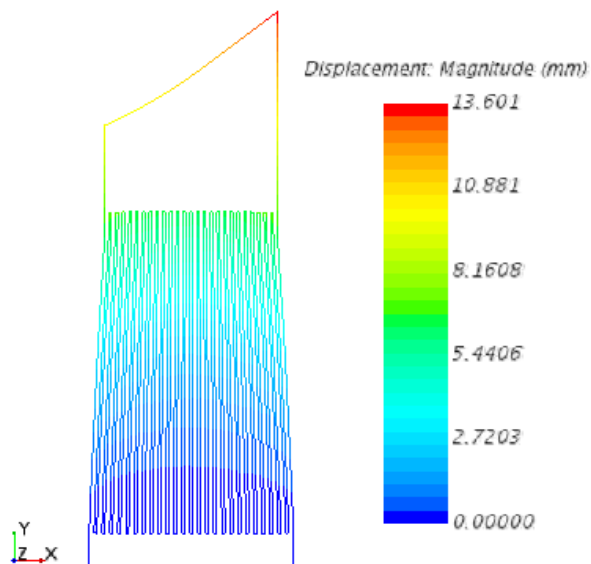


Figure 2.20 Vertical deformation map computed for the TA located in z_9 . The deformed geometry is represented on a 40:1 scale.

The maximum vertical deformation decreases when the TA is moved upward along the GS, see Figure 2.21: the z_9 position of the TA gives the lowest deformation value.

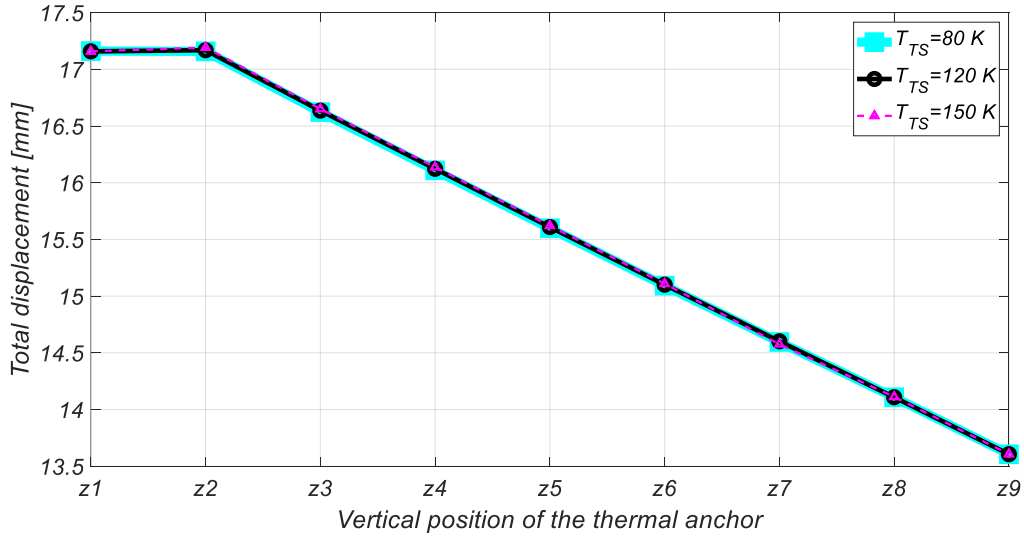


Figure 2.21. Trend of maximum deformation depending on the vertical position of the thermal anchor for each TS temperature.

In Figure 2.21, all curves are overlapped highlighting the independence of the vertical deformation on the TS temperature. Therefore, the vertical deformation reaches the same value for each TS temperature. Moreover, the displacement is slightly higher than the base case: that is due to the superposition of the refrigeration which adds a thermal deformation.

As it is possible to notice, no horizontal displacement takes place – a distortion of the computed deformation field would occur whenever a 3D computation will be done.

2.4.3. Parametric study: variable helium temperature

In this section, a more realistic thermal analysis has been performed considering the heavy effect on the temperature of the helium coolant.

Considering the TA in the position z_9 , a more in-depth study has been made for each TS temperature; the TF casing receives a thermal load around 22 W. Therefore, the analysis has been carried out for the two extreme cases. Starting from the \dot{Q}_{conv} removed by the coolant and the helium inlet enthalpy evaluated at the conditions of $T_{in} = 4.5 K$ and $p_{in} = 600 kPa$, it has been possible to calculate the outlet enthalpy as in Eq. (2.9):

$$h_{outlet} = h_{inlet} + \frac{\dot{Q}_{conv}}{\dot{m}} \left[\frac{W}{m^2 \cdot K} \right] \quad (2.9)$$

The outlet temperature has been obtained reversing the enthalpy value. Since the temperature is not uniform anymore along the pipe, the heat transfer coefficient to the coolant in the TA needs to be re-evaluated at the mean temperature between the inlet and the outlet, following the same estimation done in the first analysis. It is found that in all cases the heat transfer coefficient remains bounded in the window $100 \frac{W}{m^2 \cdot K}$ to $700 \frac{W}{m^2 \cdot K}$.

An iterative procedure is then established to assess self-consistently the heat transferred to the TA: the computed \dot{Q}_{conv} from one iteration is used to estimate the value of the helium outlet temperature in the TA, used as boundary conditions for the following iteration. The iterative procedure is performed for both the minimum and maximum value of the mass flow rate in the TA for the possible temperatures of the TS. The convergence is reached in few iterations.

The heat transferred to the TF casing is the minimum when the largest fraction of heat is removed by the TA, i.e. in the presence of the highest fluid mass flow rate, as reported in Table 2.3.

Table 2.3. Summary of the thermal load to the TF casing.

T_{TS} [K]	Q_{top} @ $T_{TA} = 4.5$ K [W]	Q_{top} @ \dot{m}_{min} [W]	Q_{top} @ \dot{m}_{max} [W]
80	22	46	8
120	25	49	11
150	30	54	16

The temperature maps related to the case of $T_{TS} = 80$ K and to $\dot{m}_{min} = 18$ g/s are reported in Figure 2.22, for the sake of completeness.

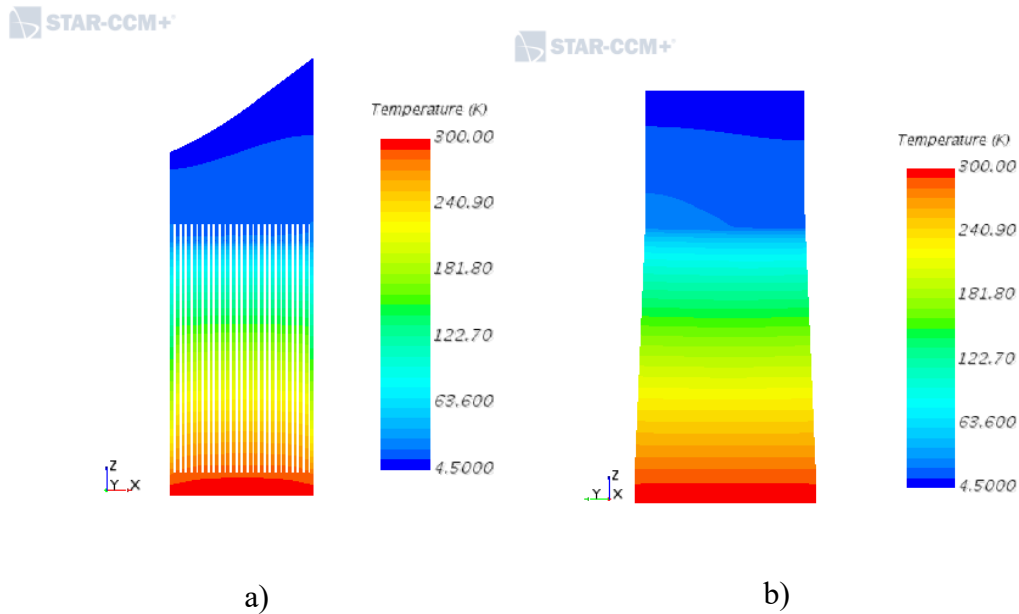


Figure 2.22 a) 2D temperature map of the GS computed on a xy cross section and c) 2D temperature map of the GS computed on a yz cross section. They refer to $T_{TS}=80$ K and $\dot{m}_{min} = 18$ g/s.

From Figure 2.22 b) it is possible to notice the impact of the variable temperature of the coolant on the structure: the GS temperature map results are no more uniform along y -axis, but increasing from the left side (where there is supposed to be the helium inlet) to the right side (where there is supposed to be helium outlet).

2.5. Second mitigation: Double Thermal Anchor application

The possible application of a second TA to the GS has been investigated: the idea is to locate that at higher temperature (TS temperature) in the lower part of the GS and the second at lower temperature (4.5 K) as it comes out from the previous study, see Figure 2.23.

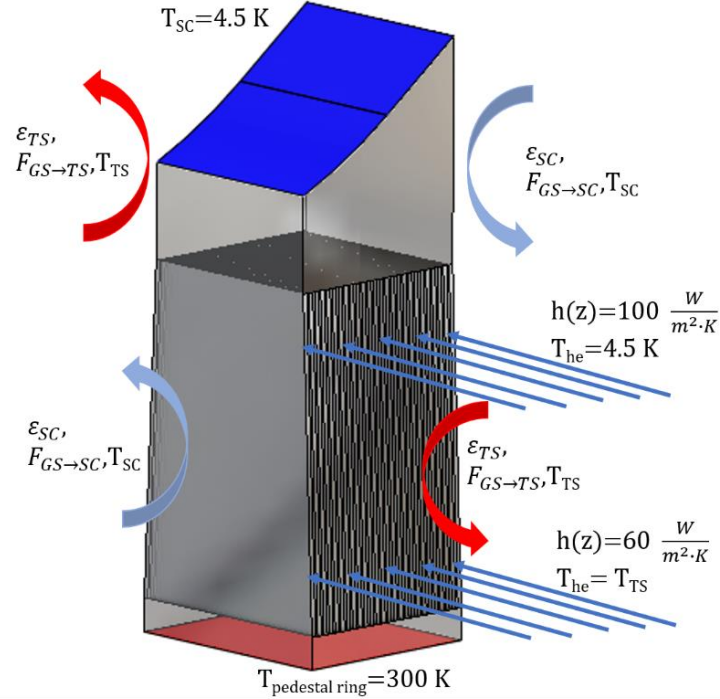


Figure 2.23 Boundary conditions for double thermal anchor problem.

In addition to what has been done previously, a second *Robin boundary condition* has been applied. The coolant outlet temperature is considered equal to the inlet one for both TAs, taking care to apply the proper heat transfer coefficient for the two TA, and namely: for the TA placed at z_1 with $T_{he} = 4.5 \text{ K}$, the value of $h = 100 \frac{\text{W}}{\text{m}^2 \cdot \text{K}}$; for the TA located at z_2 with $T_{he} = T_{TS}$ the value of $h = 60 \frac{\text{W}}{\text{m}^2 \cdot \text{K}}$, which results in a good approximation of the three possible temperatures.

2.5.1. Thermal analysis results

The analysis has been carried out for each TS temperature, imagining that the coolant for the second TA is re-routed from the TS to the GS.

The results, in terms of heat load transferred to the TF casing, show a decrease for each simulation, see Table 2.4.

Table 2.4 Comparison of the thermal load between the application of one TA and two TAs.

$T_{TS} \text{ [K]}$	$Q_{\text{top}} @ T_{TA} = 4.5 \text{ K [W]}$	$Q_{\text{top}} \text{ double TA [W]}$
80	22	6
120	25	12
150	30	20

The application of a second TA may reduce the thermal load to the casing to more than $\sim 50\%$ of the value obtained with a single TA at 4.5 K, considering the TS temperature equal to 80 K.

The computed temperature distribution for a TS temperature equal to 80 K results more uniform in the central zone and it is shown in Figure 2.24.

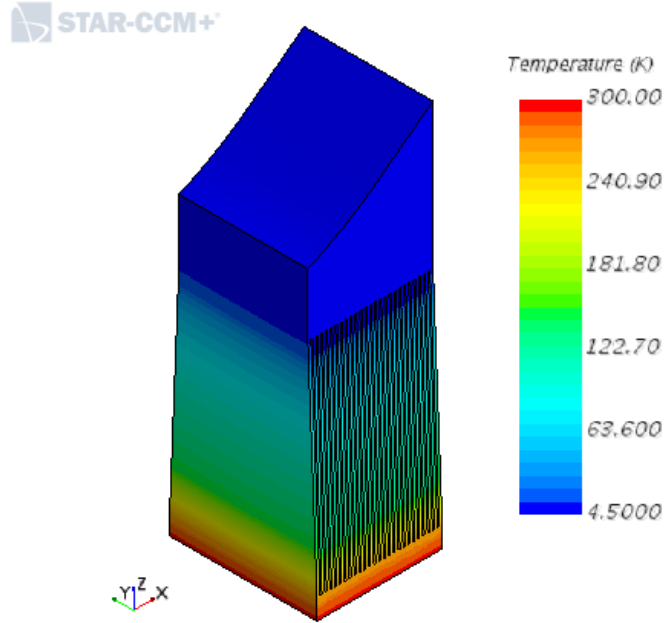


Figure 2.24 Temperature distribution computed for the GS with a double TA for $T_{TS} = 80$ K.

2.5.2. Thermal-mechanical analysis results

As regards the effect in terms of displacement, a slightly higher vertical deformation is computed, again without any horizontal distortion.

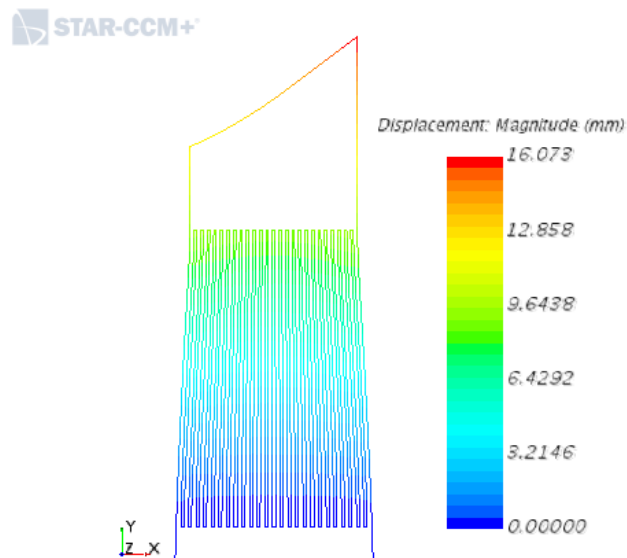


Figure 2.25 Displacement. The deformed geometry is represented on a 40:1 scale.

2.6. Preliminary conclusions

In conclusion, the conductive path constituted by the GS may give a thermal load to the TF coil casings slightly more than 1 kW for each TS temperature. Thus, a refrigeration is required.

The first approach consists on the application of a thermal anchor surrounding the GS in which SHe, re-routed from the SC cooling circuit at constant temperature of 4.5 K, flows in. Thanks to the TA, the parasitic heat load will be reduced of two orders of magnitude. A parametric analysis has been computed in order to determine the optimal location for the TA in terms of heat load to the TF coil casing and in terms of displacement. The position z_9 results the most suitable choice: $\sim 22 W$ is obtained for the TS at 80 K and $\sim 13.5 mm$ of displacement. A more in-depth study has been implemented, considering the heavy effect on the coolant.

Moreover, the beneficial effects of the application of another TA at higher temperature (re-routed from the TS) have been reported. The simulations give results of two orders of magnitude lower than the base case and of a reduction of more than 50% of the thermal load considering $T_{TS}=80 K$ with respect to the application of a TA.

Chapter 3

3. Magnet system feeders analysis⁶

3.1. Design

The magnet system feeders convey and regulate the cryogenic liquids, needed to cool and control the temperature of the magnet system, and they connect the magnets to their power supply, housing the bus-bars. Based on the ITER experience, and moving from the outside to the inside of the Tokamak, the feeder assembly of each coil consists of the following sub-units [22]: Coil-Terminal Box (CTB) and S-Bend Box (SBB), Cryostat Feedthrough (CFT), including the Vacuum Barrier (VB), In-Cryostat Feeder (ICF) with the connection to the coil terminals ('terminal joint'), see Figure 3.2. The present work focuses only on the CFT-VB sub-unit.

This analysis aims at developing a simple model to evaluate the background heat load on the Helium line feeding each TF coil in DEMO inside one of the CFT, see Figure 3.1. Since the ultimate goal is to minimize that load on the He supply line, it has been possible to concentrate on the longest CFT (at the B4 level, see Figure 3.1), the length of which is estimated in [23] to be 19.4 m (rounding to 20 m, to stick to a couple of significant figures).

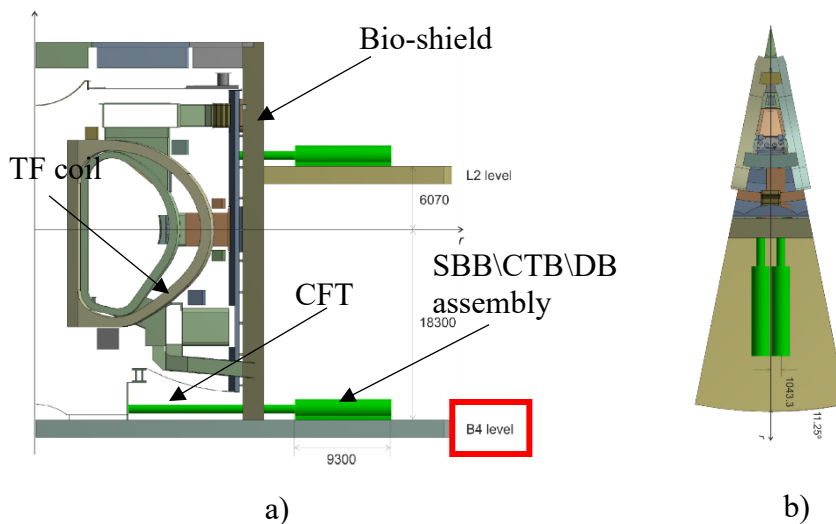


Figure 3.1 Sketch of the Cryostat Feed-Through (CFT) penetration at B4 level and L2 level in DEMO (reproduced from [23]).

⁶ Mainly based on L. Savoldi, A. Allio and S. Viarengo, "Study of the cooling phase, the thermal exchange and the layout of the cryogenic circuits", EUROfusion report EFDA_D_2NXLBX, February 2020.

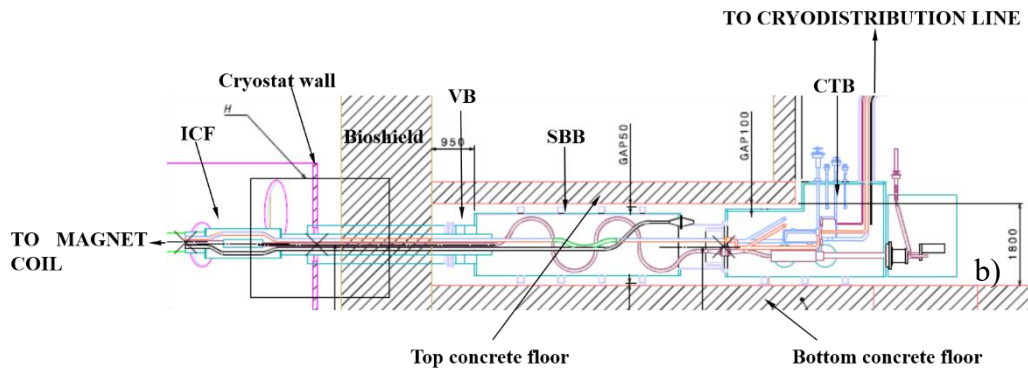


Figure 3.2 Sketch of the feeder systems reported in [24].

The inner pipe distribution within the CFT, as well as the pipe dimension, has not been set yet, so ITER design, reported in

Figure 3.3, has been used as the reference.

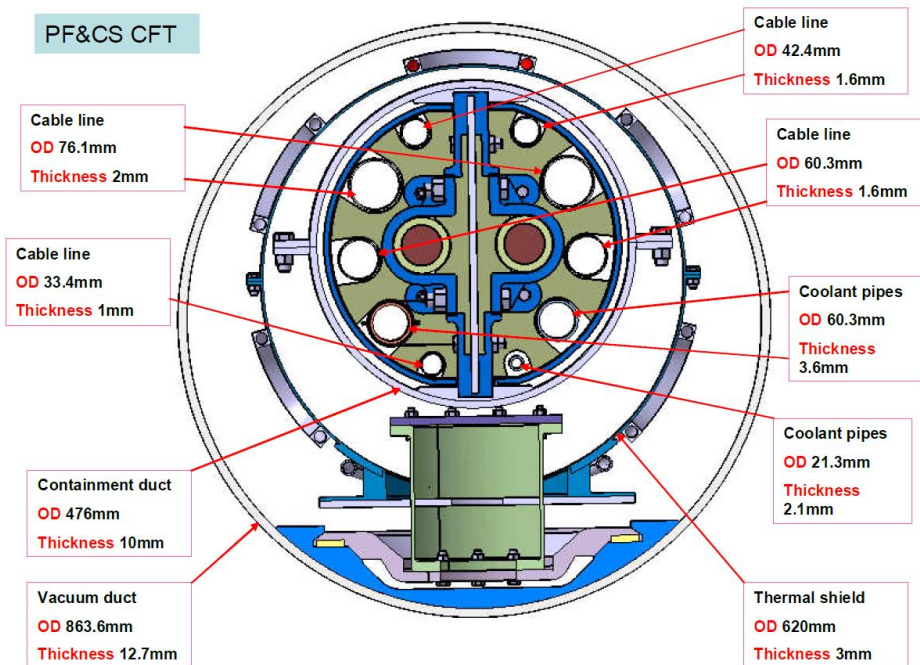


Figure 3.3 Detailed view of the ITER CFT cross-section (reproduced from [22]).

The CFT passes through the concrete bio-shield. In ITER, it is bounded by the in-cryostat joint on the coil side and the mid-joint at the SBB end, and it includes the feeder vacuum barrier, which separates the vacuum in the magnet cryostat and the vacuum in the CTB/SBB, and several cold mass supports, see Figure 3.2. The current DEMO pre-conceptual design for the vacuum barrier (1 for each feeder) and the cold mass supports (4 supports for the feeders at the B4 level [23]) are reported in

Figure 3.4 a) and in

Figure 3.4 b), respectively, following the ITER design [22].

In ITER, the containment duct of the CTB contains a separator plate, with a thermal interception to cool it, as well as the containment duct assembly, and internal supports for the BBs and cryo-pipes, see Figure 3.5, which are not foreseen at the this stage of the DEMO design.

In ITER, the Containment duct includes 4 He supply/return lines, 1 He line for the bus-bars, 2 bus-bars lines and several diagnostic penetrations, sticking to that design for the time being.

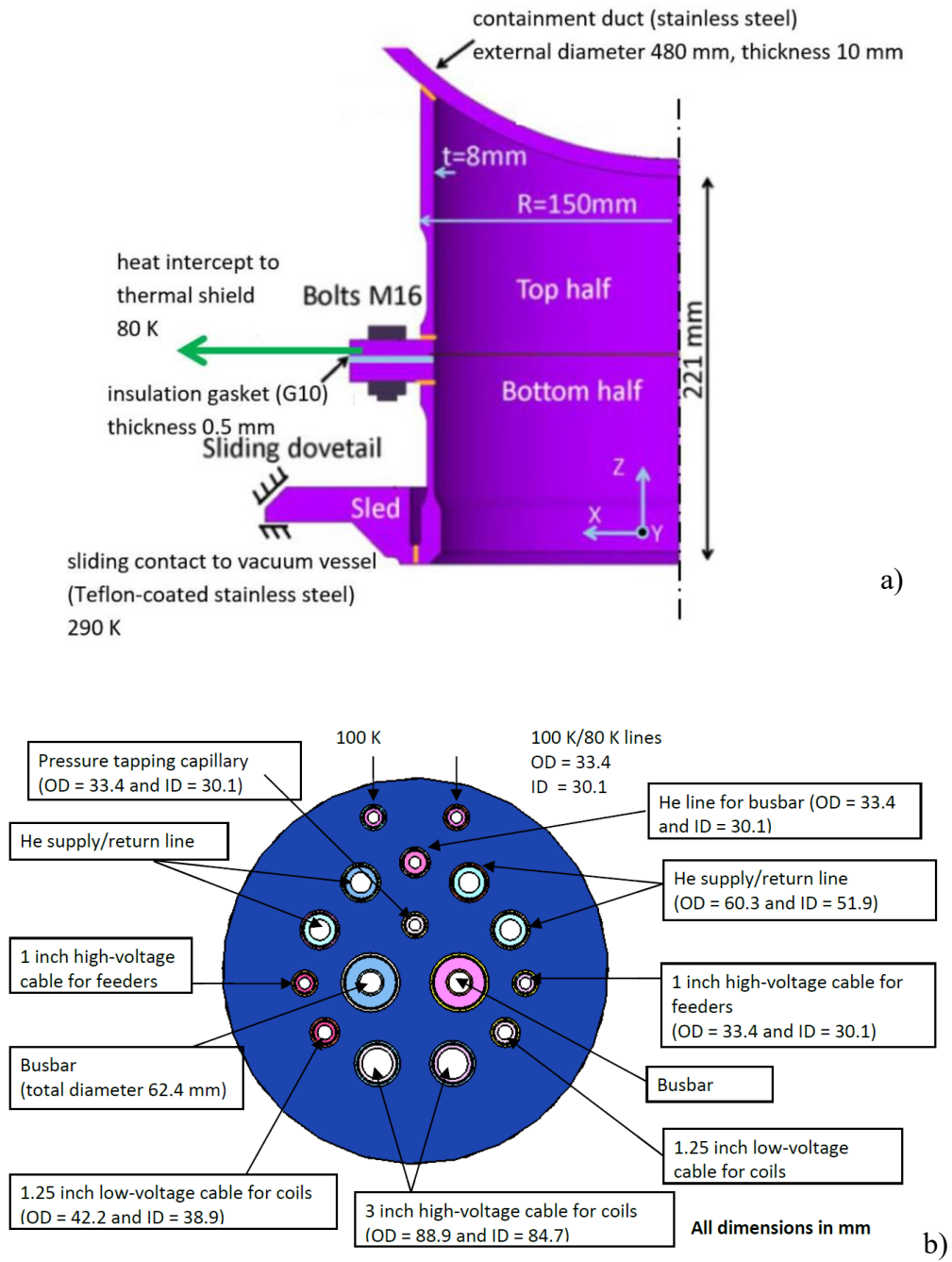


Figure 3.4 Detailed sketch of the cross section of the Cold mass support (a) and vacuum barrier (b) within an ITER CFT (reproduced from [22]).

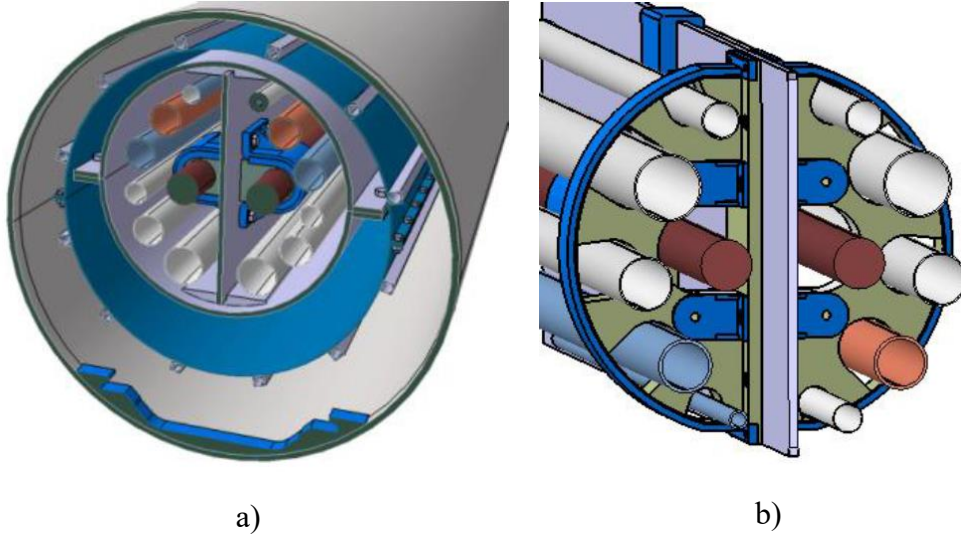


Figure 3.5 Detailed view of the Bus-Bar support (a) and cryolines support (b) within and ITER CFT (reproduced from [22]).

3.2. Thermal model

A first evaluation of the thermal load to the He supply line has been carried out by developing a simple steady-state 1D thermal model. For the SHe flowing in the pipe, it is assumed that the advection equation results from the energy balance across an infinitesimal length element of the He line, shown in Figure 3.6. Therefore, the increase in enthalpy is obtained as the product of the specific heat at constant pressure c_p , evaluated at an average temperature T , and the corresponding temperature increase $T + \frac{dT}{dx}$ (in K).

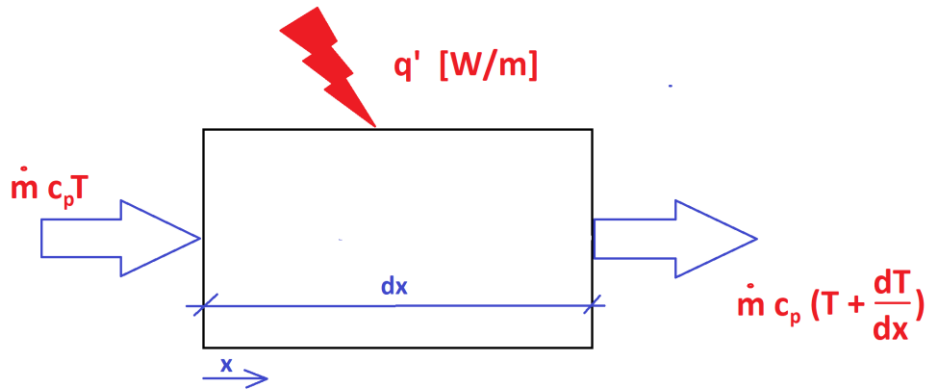


Figure 3.6 Sketch of the energy balance across an element of the He supply line, having infinitesimal length. \dot{m} is the helium mass flow rate, c_p is the specific heat at constant pressure, q' is the heat load per unit length [W/m], T is the temperature, x is the coordinate along the He pipe.

Using a simple upwind recipe for the spatial derivative, the discretized equation has been implemented in *MATLAB* (MathWorks [25]) to compute the steady-state temperature evolution in the node $i+1$ along the He pipe becomes as in Eq. (3.1):

$$T_{i+1} = T_i + \frac{q' \Delta x}{\dot{m} c_p} \quad (3.1)$$

The value of the heat load per unit length q' is computed to account for the possible different heat sources coming from what surrounds the He pipe, and namely: the thermal radiation from the Containment Duct (CD), the conduction from the Cold Mass Support (CMS) (additional load to the CD) and the conduction from the Vacuum Barrier (VB), see Figure 3.7.

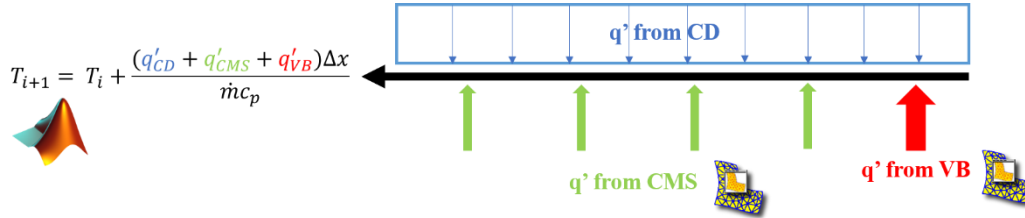


Figure 3.7 Sketch of the thermal model implemented.

The thermal radiation from the Containment Duct has been evaluated through the series of thermal resistances reported in Figure 3.8. Note that no radiative heat transfer among the pipes inside the containment duct is accounted for, since all the He lines will be approximately at the same temperature, while the ducts containing the diagnostics will be approximately at the temperature of the containment duct.

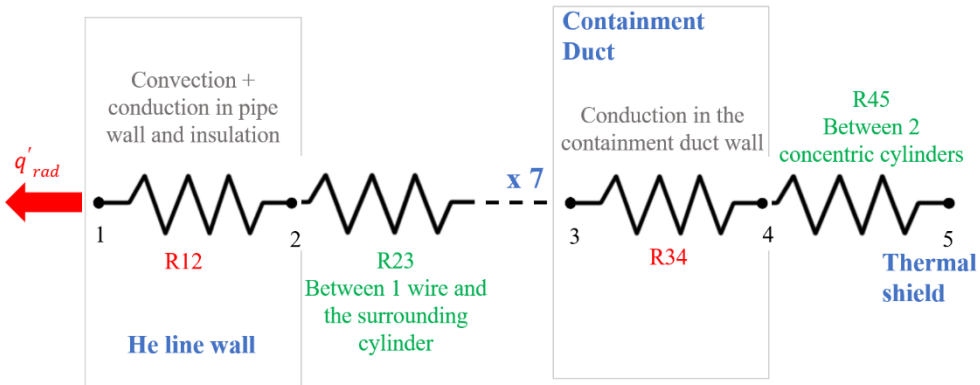


Figure 3.8 Sketch of the simple radiative model for the He supply line. The factor “7x” accounts for the number of cryogenic lines at the same temperature, namely 7.

The heat load per unit length coming from the thermal radiation q'_{rad} is computed by solving iteratively the non-linear set of equations (3.2).

$$\left\{ \begin{array}{l} q'_{rad} = \frac{T_2 - T_1}{R_{12}} \\ q'_{rad} = q_{32} \\ q_{32} = \frac{T_3 - T_2}{R_{23}} \\ 7 \times q_{32} = q_{43} \\ q_{43} = \frac{T_4 - T_3}{R_{34}} \\ q_{43} = q_{54} \\ q_{54} = \frac{T_5 - T_4}{R_{45}} \end{array} \right. \quad (3.2)$$

where q_{XY} are the heat fluxes per unit length from the node X to the node Y, and R_{XY} are the thermal resistances between the node X and the node Y, defined in Eqs (3.3-5). T1 is the helium temperature, i.e. the value of the temperature T_i from Eq. (3.1), and T5 is the TS temperature, parametrically varied from 80 K to 150 K.

$$R_{12} = \left(\frac{1}{HTC \times \pi \times D_{in_Heline}} + \frac{\log\left(\frac{D_{out_Heline}}{D_{in_Heline}}\right)}{2\pi k_{ss}} + \frac{\log\left(\frac{D_{out_Heline} - ins}{D_{in_Heline} - ins}\right)}{2\pi k_{ins}} \right) \quad (3.3)$$

$$R_{23} = \left[\pi \times D_{out_ins} \times \sigma \times (T_2^2 + T_3^2) \times (T_2 + T_3) \right]^{-1} \quad (3.4)$$

$$R_{34} = \left(\frac{\log\left(\frac{D_{out_cd}}{D_{in_cd}}\right)}{2\pi k_{ss}} \right) \quad (3.5)$$

$$R_{45} = \left[\pi \times D_{out_CD} \times \sigma \times (T_4^2 + T_5^2) \times (T_4 + T_5) \right]^{-1} \quad (3.6)$$

In Eqs (3.3) and (3.5), HTC is the convective heat transfer coefficient, computed using the Dittus-Boelter correlation [26], k_{ss} and k_{ins} are the thermal conductivity of stainless steel and insulation (Glass epoxy considered here), evaluated at 4.5 K, and the different diameters D_{in*} and D_{out*} can be found in Table 3.1.

In Equations (3.4) and (3.6), σ is the Stefan-Boltzmann constant.

The additional conductive heat load to the Containment duct, coming from the Cold mass support acts in 4 equally spaced locations along the He line. Each support has been accounted for with a 2D model in *FreeFEM++-cs* [27] as shown in Figure 3.9 (only half of the support is modelled, thanks to symmetry considerations), with an equivalent length of 0.118 m.

The SS and insulation material properties are discussed in Appendix 1: Physical properties of Stainless Steel and insulation material, while the construction of meshes in Appendix 3: Construction of meshes.

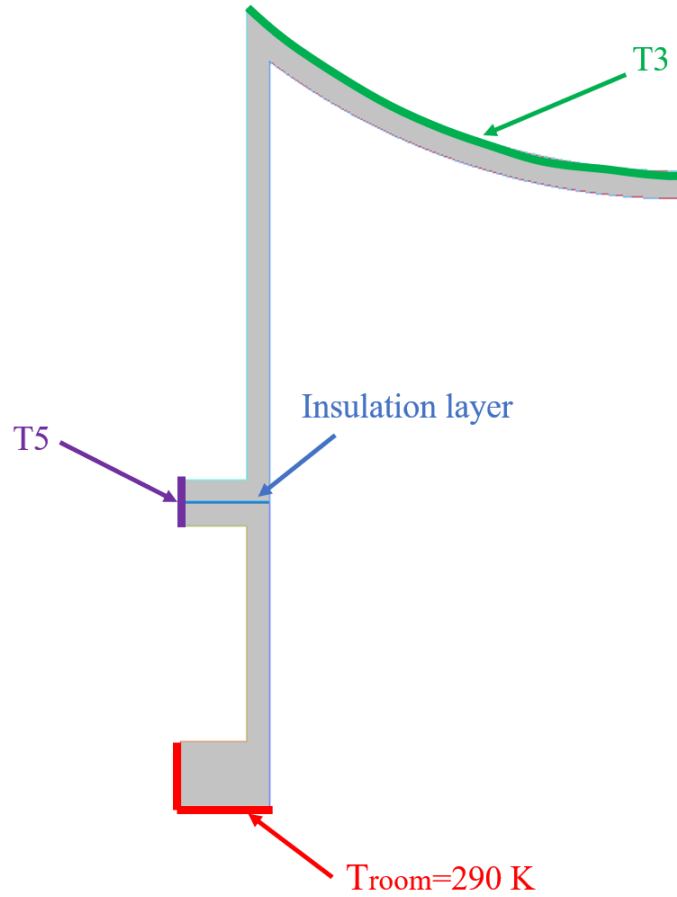


Figure 3.9 2D model of the Cold Mass support, highlighting the boundary conditions for the steady-state thermal conduction problem. The boundary condition on the top of the structure is constrained at the internal Containment duct temperature T_3 (see Figure 3.8); the thermal shield temperature T_{T5} is imposed where the support is in contact with the thermal shield, and the room temperature is imposed at the bottom of the structure.

The thermal conduction coming from the Vacuum barrier has been assumed located at $x=0$ with thickness of 30 mm [23], and modelled as shown in Figure 3.10. Note that no thermal intercepts on the feeder thermal shield, which would keep the vacuum barrier plate at 80 K (see [22] for details), is presently included in the design. The vacuum barrier contains several penetrations. In the annular region corresponding to the space between the feeder vacuum duct and the containment duct (region labelled as “R1” in Figure 3.10), two feed-throughs with helium at the thermal shield temperature (T_5 in Figure 3.8) are foreseen. In the region that would be all inside the thermal shields (region labelled as “R2” in Figure 3.10), 7 different conduits for the helium at 4.5 K are present (ITER design). The penetrations for the diagnostic are neglected at this stage.

An equivalent convective heat transfer coefficient ($U_{convective}$) to the helium at both T_5 temperature and 4.5 K has been computed through a global transmissivity, as reported in Eq. (3.7):

$$U_{convective} = \left(\frac{1}{HTC} + \frac{D_{out-*} - D_{in-*}}{2k_{ss}} + \frac{D_{out-*-ins} - D_{in-*-ins}}{2k_{ins}} \right)^{-1} \quad (3.7)$$

where HTC is the convective heat transfer coefficient, computed using the Dittus-Boelter correlation [26], k_{ss} and k_{ins} are the thermal conductivity of

stainless steel and insulation (Glass epoxy considered here), evaluated at 4.5 K, and the different diameters D_{out}^* and D_{in}^* , where * can stay for “Heline” or “Busbar”, can be found in Table 3.1.

On one side of the vacuum barrier, heat transfer by radiation occurs to the thermal shield inside the feeder (from region R1) and to the containment duct and cryogenic pipes in it (in region R2). This heat loss is accounted for as a volumetric heat sink in the thermal problem.

The SS and insulation material properties are discussed in Appendix 1: Physical properties of Stainless Steel and insulation material, while the construction of meshes in Appendix 3: Construction of meshes.

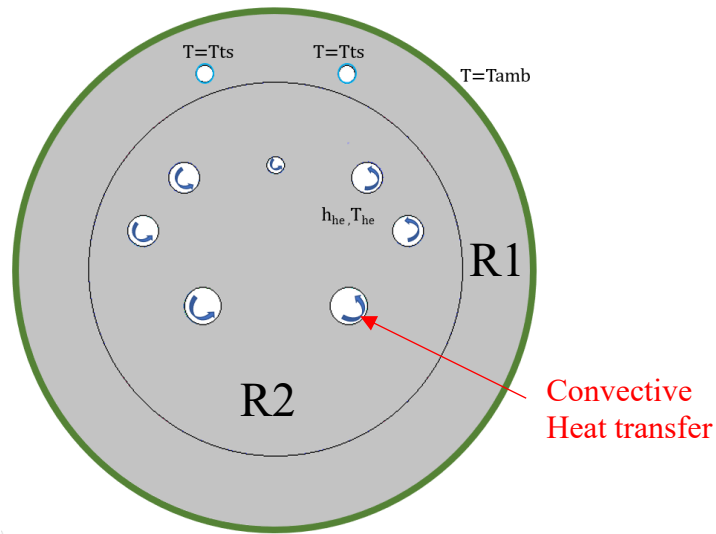


Figure 3.10 - 2D model of the Vacuum barrier, highlighting the boundary conditions for the steady-state thermal conduction problem. The room temperature is imposed on the outer circle, the Thermal Shield temperature T_{TS} is imposed on the cooling channels of the thermal shield, and convective heat transfer to Helium at 4.5 K is imposed on the outer surface of the cryogenic lines inside the thermal shield.

Table 3.1 Geometrical dimensions of quantities of interest for the present analysis

Parameter	Value
$D_{in-Helne}$	51.9 mm [1]
$D_{out-Helne}$	60.3 mm [1]
$D_{in-Helne-ins}$	60.3 mm [1]
$D_{out-Helne-ins}$	68.3 mm &
$D_{in-busbar}$	46.4 mm [2]
$D_{out-busbar}$	50.4 mm [2]
$D_{in-busbar-ins}$	50.4 mm [2]
$D_{out-busbar-ins}$	62.4 mm [2]
D_{in-CD}	460 mm [1]
D_{out-CD}	480 mm [1]

& Tentative value

3.2.1. Results

The temperature profile along the He supply line, as results from the applied model, is reported in Figure 3.11 a), for a tentative value of the He mass flow of 100 g/s. The additional heat load coming from the Vacuum Barrier and from the Cold Mass supports has been taken into account, and it corresponds to the temperature increase at the beginning of the line and along the line, respectively.

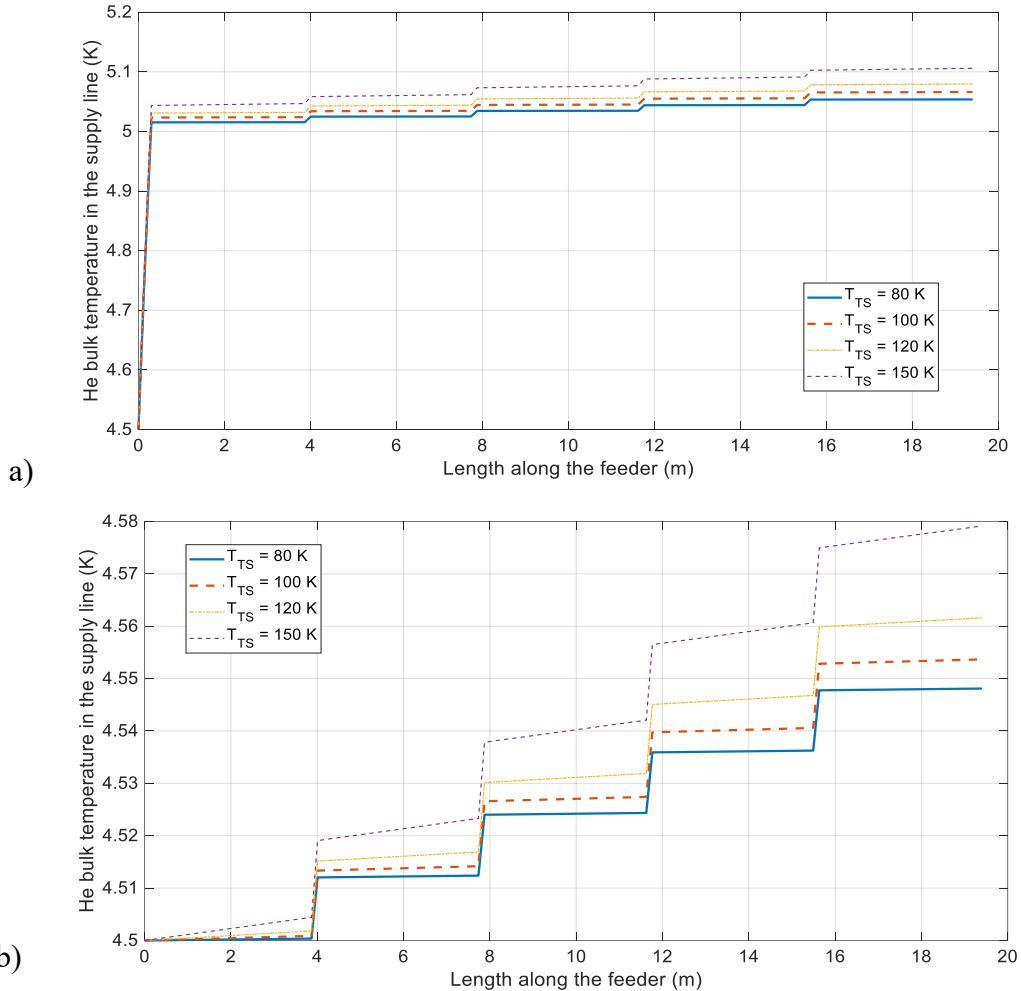


Figure 3.11 Computed temperature profile for the He along the supply line, accounting (a) and neglecting (b) the contribution of the additional heat load from the Vacuum Barrier.

The additional heat load coming from the Vacuum barrier is at least one order of magnitude larger than in ITER, see Table 3.2. Since there is no thermal intercept that cools down the entire barrier to the temperature of the TS, the average temperature of the Vacuum Barrier is much larger than the cryogenic one as shown in Figure 3.12.

The effect of the heat load coming from the radiation and from the Cold Mass supports is reported in Figure 3.11 b): the contribution of the Vacuum Barrier is neglected, for all the different possible nominal temperature values of the TS. The maximum temperature increase along the line varies from ~ 50 mK, for the minimum TS temperature, up to ~ 80 mK, for the largest value of the TS temperature.

It can be also noted from Table 3.2 that the temperature computed for the Containment Duct is far from the nominal value of 4.5 K, due to the absence of an active cooling or a thermal intercept, that would further mitigate the load to He lines.

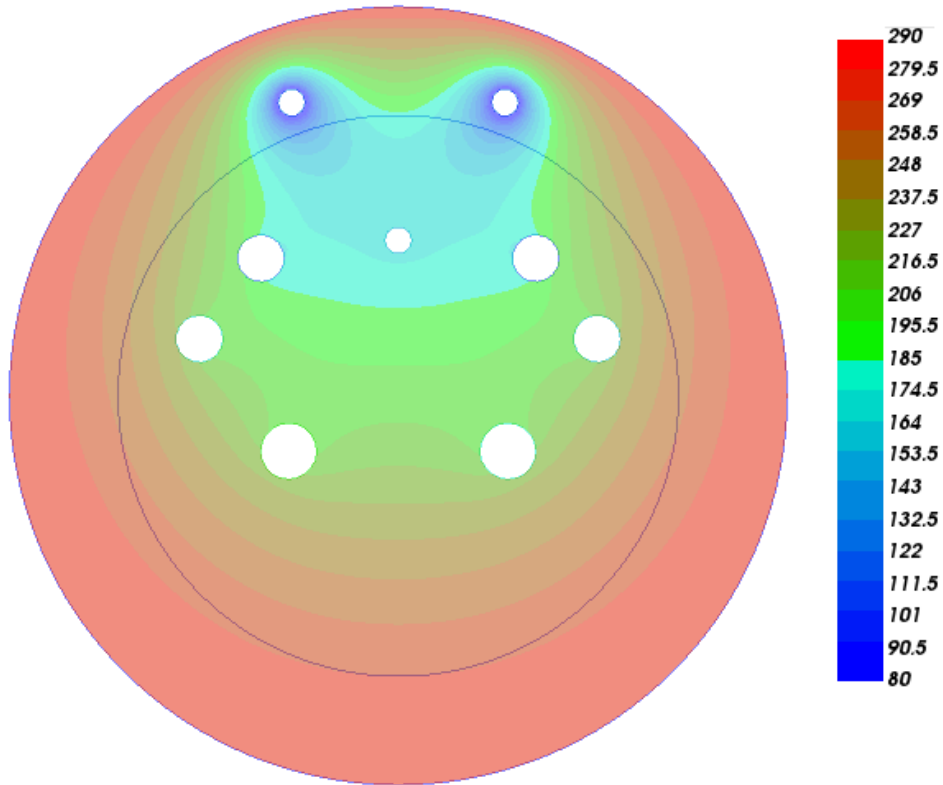


Figure 3.12 Temperature map computed for the Vacuum Barrier, with a thermal shield temperature of 80 K. The color bar reports values in K.

Table 3.2 – Computed duct temperature and additional heat load from each of the Cold Mass support and from the Vacuum Barrier, as a function of different plausible nominal temperature of the Thermal shield.

Thermal shield temperature [K]	Containment duct temperature [K]	Load from Cold Mass supports [W/m]	Load from the Vacuum barrier [W/m]
80	70	28.6	690
100	88	30.4	702
120	105	31.8	713
150	132	34.2	732

The thermal load that reaches TF coils can be evaluated through Eq. (3.8):

$$\dot{Q} = \dot{m}_{he} \cdot cp_{he} \cdot \Delta T [W] \quad (3.8)$$

where \dot{m}_{he} is the mass flow considered for the study (100 g/s), cp_{he} is the heat capacity (5.19 kJ/kg/K, evaluated at T=4.5 K and p=600 kPa) and ΔT is the

difference between the ideal temperature at which helium should reach TF coils (4.5 K) and the temperature obtained from the previous analyses, for each TS temperature.

The results are summarized in Table 3.3.

Table 3.3 Thermal load to the TF coils for each TS temperature accounting and neglecting the VB contribution

T_{TS} [K]	T_{He} (no load fromVB) [K]	Load (incl. VB) [W]	T_{He} (no load fromVB) [K]	Load (incl. VB) [W]
80	4.548	25	5.054	288
100	4.554	28	5.066	294
120	4.562	33	5.08	301
150	4.583	42	5.11	316

With the aim of maintaining the helium entering the TF coils around 4.5 K as much as possible, mitigation actions are needed to limit the temperature increase.

3.3. Preliminary conclusions

A first analysis of the static heat load on the He supply line in the DEMO TF feeders has been performed by means of a 1D steady state advection model, accounting for the radiative heat load coming from the thermal shield through the Containment Duct. The thermal bridges constituted by the Vacuum barrier and the Cold Mass supports have been locally included, estimating the load by simple 2D thermal models developed on the feeder cross section. The computed results show that:

- The Vacuum Barrier needs a thermal intercept to keep the barrier temperature close to that of the Thermal Shield, as foreseen in the ITER project [22]. That would dramatically reduce the parasitic heat load to the He supply line.
- The temperature increase along the He lines due to radiation and conduction (Cold Mass supports) is between 0.01 K and 0.05 K, for the Thermal Shield temperature increasing from 80 K to 150 K, if a reference value for the TF mass flow rate is assumed of 100 g/s.
- Since the computed temperature of the Containment Duct is very close to that of the Thermal Shield, in view of the large radiative heat transfer, an active cooling to the target value of 4.5 K would further reduce the thermal load to the He lines.

Chapter 4

4. Conclusions

The objective of the study has been the evaluation of the parasitic thermal load reaching the TF coils magnet of the EU-DEMO reactor through two different conduction channels, namely the gravitational support (GS) and the Cryostat FeedThroughs (CFT), varying parametrically the TS temperature (80 K, 120 K, 150 K).

A preliminary analysis has been carried out for both components to assess which of them is more relevant to act on. The GS represents the direct thermal contact between of the external environment at 300 K and the magnets (one for each TF coil), which must be at 4.5 K, with the risk of reducing significantly the operation temperature margin. The GS temperature distribution is influenced by radiative dissipation towards the surrounding components at lower temperature. Even though the radiation is able to remove around 28% of the entering power, the load reaching the TF coils is huge, more than 1 kW, with no strong variation when different possible TS temperatures are considered. Concerning the CFT (one for each TF coil), instead, the estimation of the that thermal load has been implemented considering, first, the contribution of only the Cold Mass Support (the structural element needed to sustain the He lines every few meters of the lines) and, then, also the Vacuum Barrier conductive effect (which has a significant impact). The two cause the helium temperature increase before it can reach the magnets for cooling. The higher the TS temperature, the higher the amount of heat entering directly the magnets in the form of additional enthalpy of the inlet coolant: neglecting the VB contribution, that varies from 25 W (for $T_{TS}=80$ K) to 42 W (for $T_{TS}=150$ K), otherwise from 288 W to 316 W. Results show that the parasitic load to the GS is an order of magnitude higher than the CFT: therefore, more analyses have been carried out for mitigation actions on it. Moreover, a thermo-mechanical study for the GS has been implemented to estimate the additional displacement that could be due to the thermal field generated by the TA.

As first intervention, the application of a thermal anchor (TA) surrounding the GS, based on the ITER design, has been taken into account. The refrigeration occurs thanks to SHe at 4.5 K re-routed from the SC cooling system and the study aims at finding its optimal location. Nine different positions have been considered: simulations show that the TA removes most of the entering power (ranges between 80-98% depending on its position), independently on TS temperature, and moving upward the TA, lower will be the heat reaching the TF coils. The minimum thermal load to the casing is obtained for the TS at 80 K and the thermal anchor at z_8 , ~ 20 W. Nevertheless, the location of the TA at the top position z_9 has mechanical advantages, with an almost comparable heat removal capability and load (~ 22 W), so it has been considered the most suitable choice. Considering that first action, the parasitic thermal load has been reduced of two order of magnitude. Moreover, for the same configuration, a thermo-hydraulic analysis

considering the heavy effect on the temperature of the helium coolant has been implemented.

The second approach consists on the addition of a second TA located in the lower zone of the GS with helium flowing at higher temperature (the TS one). The heat load transferred has a decrease for each simulation: it will be reduced more than ~50%, considering the TS equal to 80 K.

4.1. Future perspectives

The study presented in this thesis has been carried out as a contribution to the design of components of the future EU-DEMO, which is expected to be constructed for 2050s. Therefore, the idea is to determine a methodologic approach to minimize the parasitic load reaching magnets, which must be at temperature of ~ 4.5 K to guarantee the superconductivity. The maintenance of a such low temperature is fundamental for good performances of the machine, and, furthermore, regarding the low temperature heat transfer also small amount of heat exchanged can be relevant. The future perspective is to attempt to define a comprehensive model to take into account the three different paths for parasitic heating from the environment, constituted by the GS, the CFT and the current leads (CL).

As regarding the final design of the GS, a coupling with the detailed analysis of the temperature distribution in the TF casing, computed by, e.g., the 4C code [28], will guarantee a self-consistent evaluation of the conductive load to the TF casing.

Concerning the CFT, the computed results highlight the need for an active refrigeration of the containment duct, in order to guarantee the He temperature entering the TF coils as close as possible to 4.5 K, limiting the increase at the acceptable value of 10 mK. In perspective, the application of a thermal intercept, as in ITER project, for the VB may drastically reduce the heat load aiming to maintain the temperature of the vacuum barrier close to the TS one.

The current leads induce a thermal load of electrical nature, due to Joule effect, that enters directly the superconducting Bus-Bar. A suitable design of the current lead heat exchanger, that removes part of that load, is undergoing. Since the BB passes into the CFT as well as the He line, a proper reduction of the load to the latter would also be beneficial in reducing the load along the Bus-Bar.

Appendix 1: Physical properties of Stainless Steel and insulation material

Due to the huge temperature gradient the thermal and mechanical properties cannot be considered negligibly temperature dependent.

- *Thermal conductivity:*

$$k_{ss} = \frac{A \cdot T}{(a + T)^{n_a}} + \frac{B \cdot T^2}{(b + T)^{n_b}} + \frac{C \cdot T^3}{(c + T)^{n_c}} + \frac{D \cdot T^4}{(d + T)^{n_d}} \quad (5.1)$$

where:

- The coefficients are specific for the material;
- The temperature is the one evaluated in the appropriate node.

- *Specific heat:*

$$c_{p_{ss}} = \frac{A \cdot T}{(a + T)^{n_a}} + \frac{B \cdot T^2}{(b + T)^{n_b}} + \frac{C \cdot T^3}{(c + T)^{n_c}} + \frac{D \cdot T^4}{(d + T)^{n_d}} \quad (5.2)$$

where:

- The coefficients are specific for the material, but different from the previous ones;
- The temperature is the one evaluated in the appropriate node.

That formula is valid only in a range between 1 K and 1253 K. Therefore, if the temperature is the lower than the minimum one:

$$c_{p_{ss}} = 0.498 \cdot T + 3.71 \cdot 10^{-4} \cdot T^3 \quad (5.3)$$

Instead, if the temperature is higher than the maximum one:

$$c_{p_{ss}} = A' \cdot T + A'' \cdot T^3 \quad (5.4)$$

where A' and A'' are suitable constants.

- *Density:*

Due to the lack of information, it has been considered constant and equal to $7900 \frac{kg}{m^3}$.

- *Thermal expansion coefficient:*

Data for the thermal expansion are reported in [29] and they were re-scaled to $\Delta L/L = 0\%$ at the reference temperature 923 K.

According to the recommended dataset, the thermal expansion follows the next equations:

- From 0 K to 293 K, with $\Delta L = 0$ at 20 °C, $\frac{\Delta L}{L}$ in % and T in K:

$$\frac{\Delta L}{L} = -0.296317 - 0.2609 \cdot 10^{-3} \cdot T + 7.1329 \cdot 10^{-6} \cdot T^2 - 9.5251 \cdot 10^{-9} \cdot T^3 \quad [\%] \quad (5.5)$$

- From 293 K to 1500 K, with $\Delta L = 0$ at 20 °C, $\frac{\Delta L}{L}$ in % and T in K:

$$\frac{\Delta L}{L} = -0.03381 + 1.6831 \cdot 10^{-3} \cdot (T - 273) + 3.6404 \cdot 10^{-7} \cdot (T - 273)^2 - 2.3028 \cdot 10^{-12} \cdot (T - 273)^3 \quad [\%] \quad (5.6)$$

For the simulations, the thermal expansion coefficient is required; considering that it is defined as:

$$\alpha = \frac{\Delta L}{L} \cdot \frac{1}{\Delta T} \left[\frac{1}{^\circ\text{C}} \right] \quad (5.7)$$

In the previous equations $\Delta T = T - T_0$, where T_0 is the temperature in which the expansion is null (in that case 293 K).

- *Elastic modulus and Poisson's coefficient*⁷:

Data for the elastic modulus and the Poisson's coefficient are again reported in [29]. According to the recommended dataset:

- For $T > 173$ K:

$$E = 200.4 - 8.1221 \cdot 10^{-2} \cdot (T - 273) \quad [\text{GPa}] \quad (5.8)$$

$$\nu = 0.291 + 7.169 \cdot 10^{-5} \cdot (T - 273) \quad (5.9)$$

- For $T < 173$ K:

$$E = 208.5 \quad [\text{GPa}]$$

$$\nu = 0.284$$

⁷ In the specific case, the GS will be made of SS 304LN. The thermal expansion coefficient, the elastic modulus and the Poisson's coefficient polynomials reported in [29] are related to the SS 316LN, but that properties have been checked in the range 4-300 K with the 304LN one, as stated in [29]; moreover, there were chosen following the recommended.

Appendix 2: Modeling the heat transfer by radiation for the GS

The view factor represents the proportion of the radiation which leaves a surface that strikes another one; it depends on the geometries and the respective distances between the two faces.

Figure 4.1 reports one-sixteen of the entire geometry, as far as the TF system is considered.

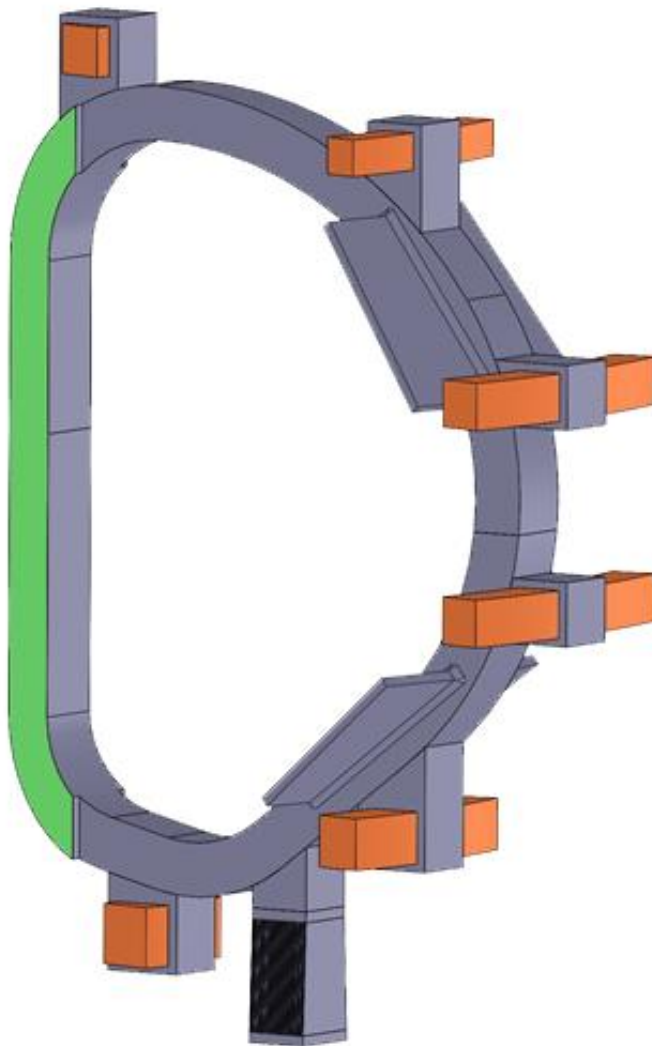


Figure 4.1 Schematic view of one TF coil [30].

For the determination of the view factor, the dimension of each component and its distance from the gravity support has been considered. Due to the complex geometry, the view factor has been evaluated with the help of the chart in Figure 4.2.

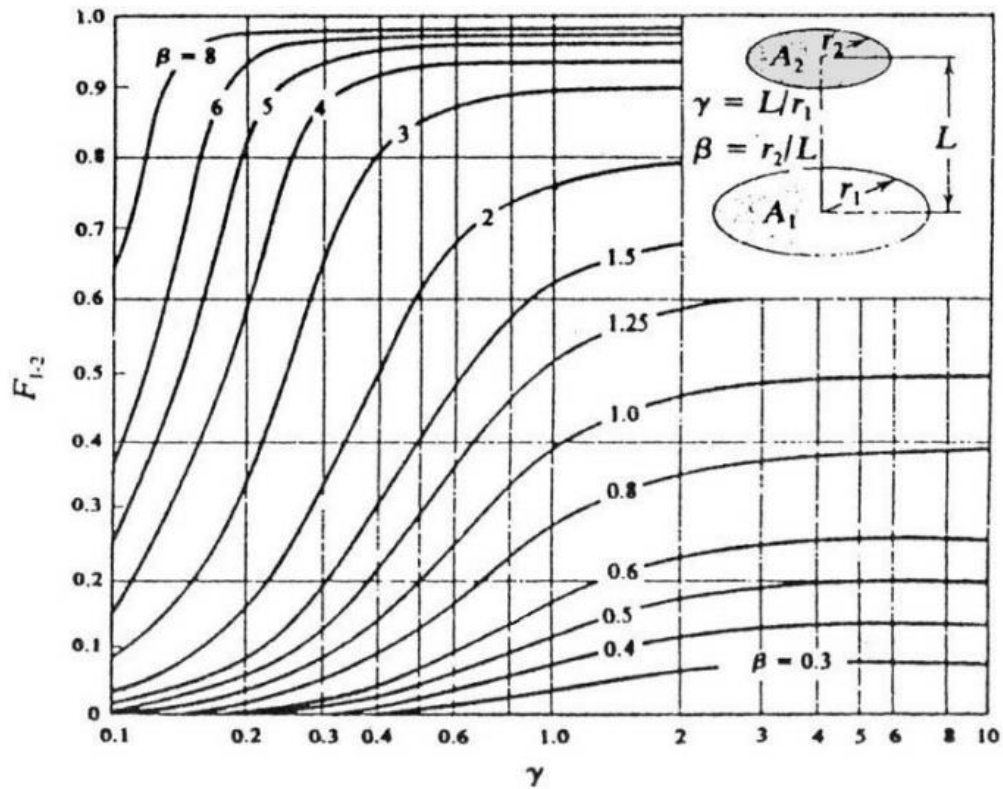


Figure 4.2. View factor chart, from [31].

Actually, the surfaces taken into account are rectangular. Therefore, the equivalent radius has been considered.

- Evaluation $F_{GS \rightarrow TS}$ on the lateral side

From the available sketch, the distance between the object and vacuum vessel has been approximated as a one-sixth of the width of gravity support. Therefore:

$$L \cong 0.3 \text{ m}$$

$$r1 \cong 4.6 \text{ m} \quad \longrightarrow$$

$$\beta \cong 7 \text{ and } \gamma \cong 0.1$$

$$r2 \cong 2.3 \text{ m}$$

Finally, from the chart:

$$F_{GS \rightarrow TS} = 0.5$$

- Evaluation $F_{GS \rightarrow magnet}$ on the back side

From the CAD, it has been possible to evaluate precisely the dimension of the different part and the distance.

Therefore:

$$L \cong 2.1 \text{ m}$$

$$r1 \cong 1.5 \text{ m} \quad \longrightarrow$$

$$\beta \cong 1 \text{ and } \gamma \cong 1.38$$

$$r2 \cong 2.3 \text{ m}$$

Finally, from the chart:

$$F_{GS \rightarrow SC} = 0.4$$

- Evaluation $F_{GS \rightarrow magnet}$ on the front side

As before, the use of the CAD has been useful for the determination of the lengths. Therefore:

$$L \cong 1.44 \text{ m}$$

$$r1 \cong 2.6 \text{ m} \quad \longrightarrow \quad \beta \cong 1.6 \text{ and } \gamma \cong 0.5$$

$$r2 \cong 2.3 \text{ m}$$

Finally, from the chart:

$$F_{GS \rightarrow SC} = 0.4$$

Actually, the GS zones, which are not exposed to magnets or to the TS, face an ambient at the TS temperature; thus, there is another contribution to heat dissipation by radiation. Simulations have been compared considering TA at z_9 with view factors equal to 1 and those calculated above: the comparison shows that the view factor impact on the parameter of interest, \dot{Q}_{top} , is negligible, with a variation of only 5%. Therefore, to be conservative, it has not been considered in simulations.

Appendix 3: Construction of meshes

Mesh for the GS 3D thermal analysis

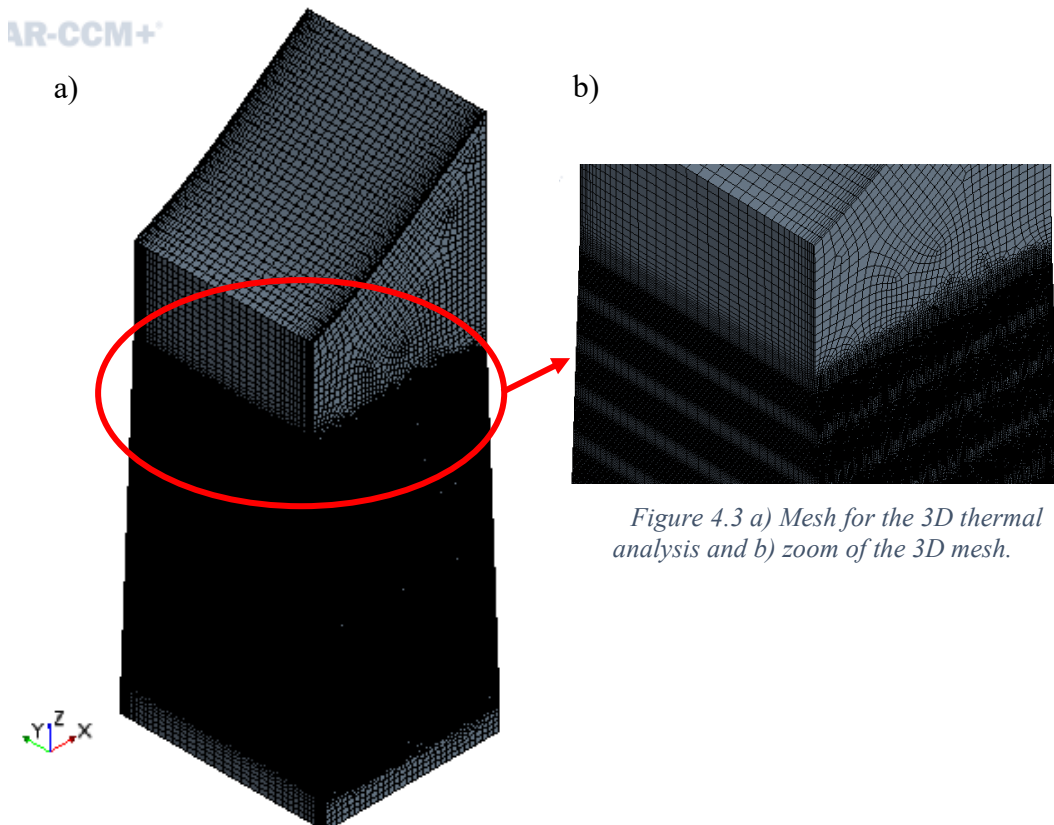
For the thermal analysis a 3D mesh of the GS has been implemented, constructed with prismatic elements characterized by a quadrilateral base, which makes the mesh lighter.

In order to optimize the calculation, the mesh is finer in the zones in which the convection boundary condition with a temperature of 4.5 K is applied; in fact, the largest gradient temperature is present there. The position considered are:

- 1) $z = 0.42 - 0.44\text{ m}$
- 2) $z = 0.70 - 0.72\text{ m}$
- 3) $z = 0.98 - 1.00\text{ m}$
- 4) $z = 1.26 - 1.28\text{ m}$
- 5) $z = 1.54 - 1.56\text{ m}$
- 6) $z = 1.82 - 1.84\text{ m}$
- 7) $z = 2.10 - 2.12\text{ m}$
- 8) $z = 2.38 - 2.40\text{ m}$
- 9) $z = 2.66 - 2.68\text{ m}$

The mesh is structured along the depth: that means that it has been translated along the depth of the GS but close the external surfaces the layers are denser in order to better describe the temperature gradients due to the different boundary conditions.

The mesh, for which the grid-independence of the results have been checked, is reported in Figure 4.3.



Mesh for the GS 2D thermal-mechanical simulation

For the thermal-mechanical study a 2D geometry has been considered.

The mesh is characterized by triangular-based elements with a refinement along all the region of the plates, because it will be the zone which will suffer more the deformation. It is finer close to the boundary, especially to the top one which is at lower temperature and where the stress is concentrated.

Moreover, it has been necessary to refine more in the neighborhood of the plate corners due to the sharp change of the geometry which implies a stress concentration.

The mesh, for which the grid-independence of the results have been checked, is reported in Figure 4.4.

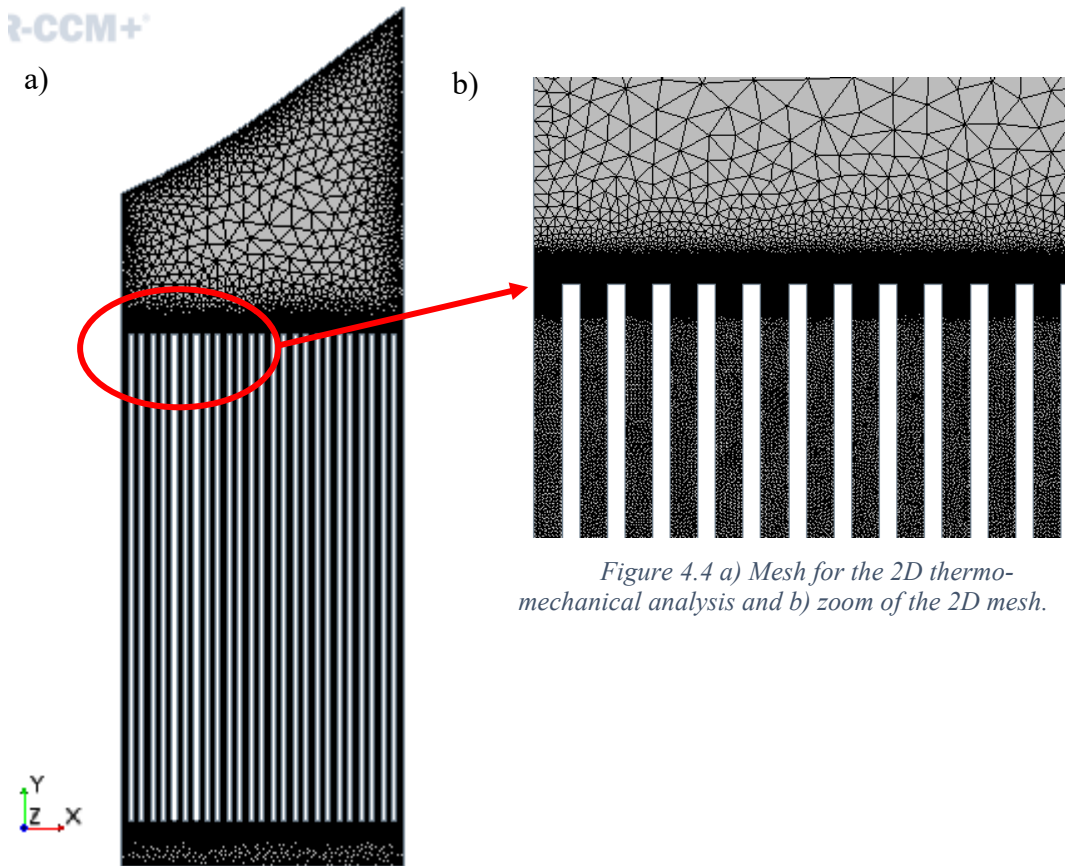


Figure 4.4 a) Mesh for the 2D thermo-mechanical analysis and b) zoom of the 2D mesh.

Mesh for the 2D Cold Mass Support analysis

Thanks to the symmetry of the problem, only half of the Cold Mass support has been modelled. Taking care of having enough nodes on the thin insulation layer the mesh, for which the grid-independence of the results have been checked, is reported in Figure 4.5.

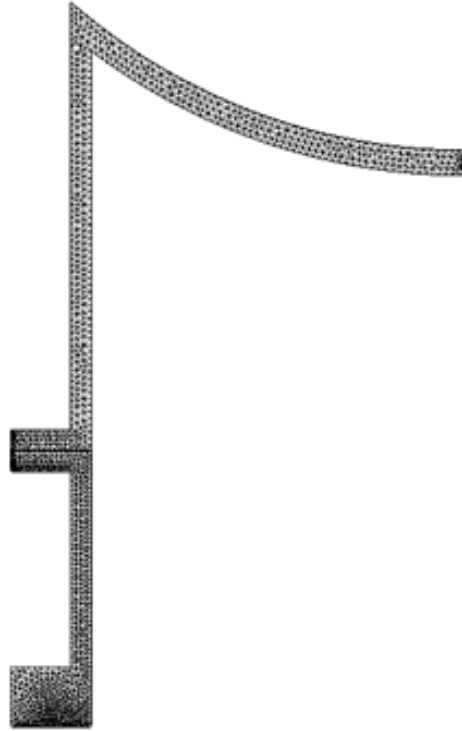


Figure 4.5 2D mesh for the Cold Mass Support implemented in FreeFEM++-cs.

Mesh for the 2D Vacuum Barrier

A uniform mesh has been constructed for the VB analysis. The mesh, for which the grid-independence of the results have been checked, is reported in Figure 4.6.

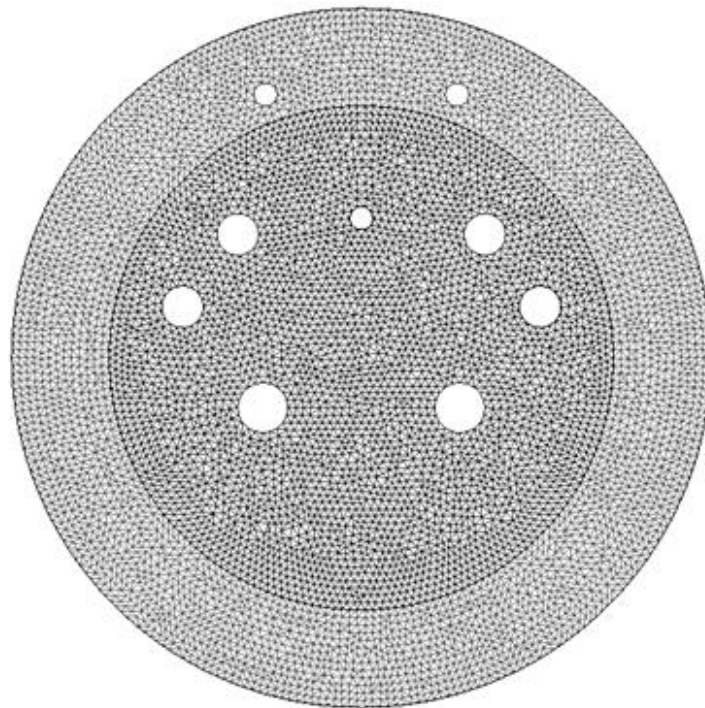


Figure 4.6 2D mesh for the Vacuum Barrier.

Appendix 4: Evaluation of the heat transfer coefficient to the TA pipes

The estimation of the equivalent heat transfer coefficient has been qualitatively implemented starting from the thermal and physical properties of the helium evaluated at inlet temperature of 4.5 K and inlet pressure of 600 kPa and the conductive resistance of the pipe in which it flows through both for the minimum and the maximum mass flow rate, respectively $\dot{m}_{min} = 18 \text{ g/s}$ and $\dot{m}_{max} = 145 \text{ g/s}$.

According to the characteristic pipe diameters found in catalogues and given the gap between two plates of 22.56 mm, an inner diameter of 16.6 mm has been considered with a thickness of 2.35 mm.

Therefore, it has been possible to calculate the two velocities:

$$v_{min} = \frac{\dot{m}_{min} \cdot A_{cross}}{\rho_{he}} \left[\frac{m}{s} \right] \quad (6.1)$$

$$v_{max} = \frac{\dot{m}_{max} \cdot A_{cross}}{\rho_{he}} \left[\frac{m}{s} \right] \quad (6.2)$$

Then, Reynolds and Prandtl numbers have been evaluated as:

$$Re = \frac{\rho_{he} \cdot v \cdot d_{tube}}{\mu_{he}} \quad (6.3)$$

$$Pr = \frac{\mu_{he} \cdot c_{p_{he}}}{k_{he}} \quad (6.4)$$

For each velocity, the helium is in turbulent flow.

The evaluation of the helium heat transfer coefficient has been carried out thanks to the Dittus-Boelter correlation and the definition of the Nusselt number:

$$Nu = 0.023 \cdot Re^{0.8} \cdot Pr^{0.4} \quad (6.5)$$

$$Nu = \frac{h_{he} \cdot d_{pipe}}{k_{he}} \rightarrow h_{he} = \frac{Nu \cdot d_{pipe}}{k_{he}} \left[\frac{W}{m^2 \cdot K} \right] \quad (6.6)$$

while the conductive resistance of the pipe has been approximated (planar geometry instead of cylindrical shell) as:

$$R_{cond} = \frac{thickness}{k_{ss}} \left[\frac{K \cdot m^2}{W} \right] \quad (6.7)$$

As a first hypothesis, the outlet temperature has been considered as equal to the inlet one.

The convective resistances can be written as:

$$R_{conv_{min}} = \frac{1}{h_{max}} \quad (6.8)$$

$$R_{conv_{max}} = \frac{1}{h_{min}} \quad (6.9)$$

Therefore, the equivalent thermal resistance is given by the sum of the convective and conductive ones, since the two are in series:

$$R_{eq_{min}} = R_{cond} + R_{conv_{min}} \quad (6.10)$$

$$R_{eq_{max}} = R_{cond} + R_{conv_{max}} \quad (6.11)$$

Finally, the equivalent heat transfer coefficient is given by:

$$h_{eq_{min}} = \frac{1}{R_{eq_{max}}} \cong 270 \left[\frac{W}{m^2 \cdot K} \right] \quad (6.12)$$

$$h_{eq_{max}} = \frac{1}{R_{eq_{min}}} \cong 601 \left[\frac{W}{m^2 \cdot K} \right] \quad (6.13)$$

Different thicknesses have been explored to catch better the influence of the resistance conduction: the higher the thickness, the higher the resistance.

Bibliography

- [1] S. P. S. Inc., Star-CCM+ User's Guide v 14.06, Plano, TX, USA, 2019.
- [2] International Energy Agency, Key world energy statistics, 2019.
- [3] International Energy Agency, Energy Access Outlook, 2017.
- [4] F. Romanelli and e. al., "Fusion Electricity. A Roadmap to the Realisation of Fusion Energy," 2012. [Online]. Available: https://www.euro-fusion.org/fileadmin/user_upload/EUROfusion/Documents/Roadmap.pdf.
- [5] EUROfusion, "The demonstration power plant: DEMO," [Online]. Available: <https://www.euro-fusion.org/programme/demo/>.
- [6] B. Labit, "Tokamak electron heat transport by direct numerical simulation of small scale turbulence," 2002. [Online]. Available: https://www.researchgate.net/publication/280790934_Tokamak_electron_heat_transport_by_direct_numerical_simulation_of_small_scale_turbulence.
- [7] "IPP," [Online]. Available: <https://www.ipp.mpg.de/w7x>.
- [8] "ITER," [Online]. Available: <https://www.iter.org/proj/inafewlines>.
- [9] "ENEA-Fusione," [Online]. Available: <http://www.fusione.enea.it/WHAT/fusion5.html.it>.
- [10] T. Markovic. [Online]. Available: https://www.researchgate.net/publication/312604149_Measurement_of_Magnetic_Fields_on_GOLEM_Tokamak/figures.
- [11] G. D'amico, L. Reccia, A. Portone, C. T.J. Jong and N. Mitchell, "ITER TF Magnet System Analyses in Faulted Conditions," 2016.
- [12] R. Zanino, R. Bonifetto and L. Savoldi, "4C code Analysis of High-Margin Quench Propagation in a DEMO TF Coil".
- [13] R. Zanino, R. Bonifetto, L. Muzzi, G. Nallo, L. Savoldi and S. Turtù, "Development of a Thermal-Hydraulic Model for the European DEMO TF Coil," 2016.
- [14] K. Sedlak, V. Anvar, N. Bagrets, M. Biancolini, R. Bonifetto, F. Bonne, D. Boso, A. Brighenti, P. Bruzzone, G. Celentano and e. al., "Advance in the conceptual design of the European DEMO magnet system," *Superconductor Science and Technology*, 2020.
- [15] G. Li, X. Huang, P. Bauer, L. Fang, J. Wang, C. Wang, Z. Dai, C. Liu, Z. Gong, N. Clayton, R. Piccin, C.-y. Gung, T. Zhou, K. Ding, C. Liu, K.

- Lu, Y. Song and E. Niu, "Development and qualification of ITER current lead electrical insulation," *Fusion Engineering and Design*, 2019.
- [16] R. Guarino and R. Wesche, "Final report MAG-2.4-T007: Extra - Sizing and preliminary design of feeders," 2020.
- [17] F. Nunio, "1st DEMO Magnets Design Progress Review Meeting," 2019.
- [18] M. Coleman, "Definition of the external static radiative and conductive heat loads on the TF coil casing," 2016.
- [19] D. Boso, *Private communication*, January 2020.
- [20] Z. Sun, P. Li, H. Wei, L. Sun, T. Zhang and B. Hou, "Study on the heat exchange efficiency of ITER GS thermal anchor," *Fusion Engineering and Design*, 2017.
- [21] A. Brighenti, R. Bonifetto, L. Savoldi, R. Zanino and A. Zappatore, "Thermal hydraulic analysis of the 2016 design of the most critical PF WP," 2018.
- [22] P. e. a. Bauer, "ITER DDD 11-6 Feeders, CTBs and current leads," 2011. [Online]. Available: <https://user.iter.org/> .
- [23] R. Guarino, "MAG-2.4-T007 inputs for PoliTO," *SPC internal reports*, 14-11-2019.
- [24] A. K. Sahu, "DESIGN DESCRIPTION DOCUMENT FOR THE VACUUM BARRIERS OF THE MAGNET FEEDERS," 2011.
- [25] MathWorks, [Online]. Available: <https://it.mathworks.com/help/matlab/>.
- [26] F. Incropera, D. DeWitt, T. Bergam and A. Lavine, "Foundation of heat transfer," *Wiley & Sons*.
- [27] "FreeFEM Manual," [Online]. Available: <http://www3.freefem.org/ff++/ftp/old-v1/full-ff++-manual.pdf>.
- [28] L. Savoldi, F. Casella, B. Fiori and R. Zanino, "The 4C code for the cryogenic circuit conductor and coil modeling in ITER," *Cryogenics*, 2010.
- [29] H. R. E. S. P. Bauer, "EFDA Material Data Compilation for Superconductor Simulation," 2007.
- [30] D. Boso, *Private communication*, 2019.
- [31] "https://www.unirc.it/documentazione/materiale_didattico/599_2011_296_16965.pdf," [Online].